CHALMERS
UNIVERSITY OF TECHNOLOGY

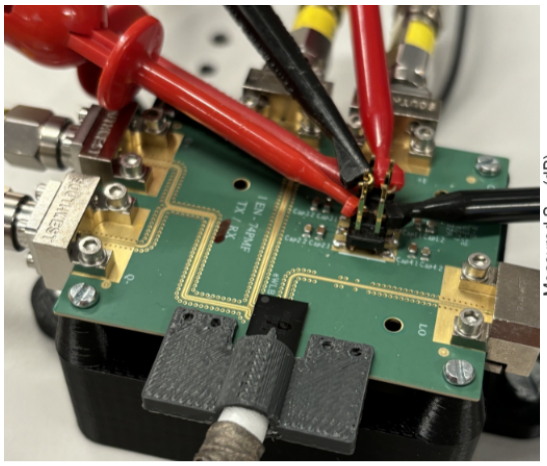

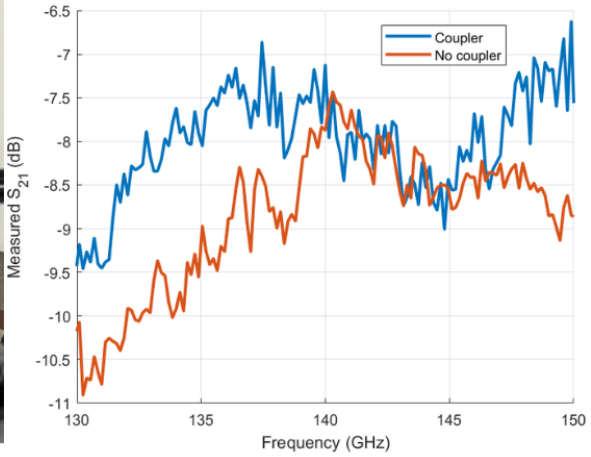

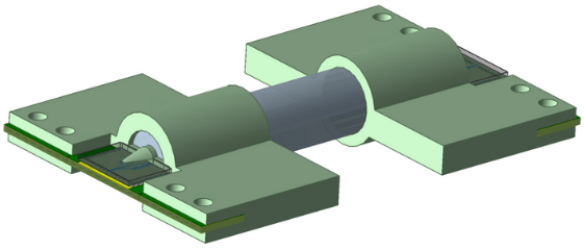

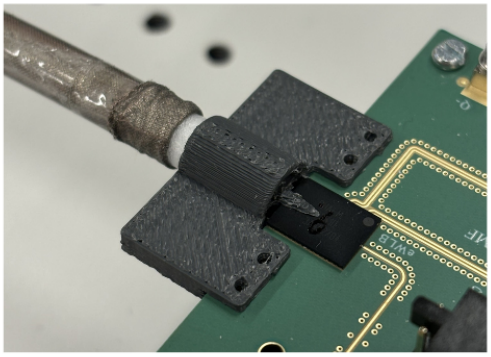

D-Band Transition from eWLB to Polymer Microwave Fiber:

Design, Fabrication, and Characterization

Master's thesis in Wireless, Photonics and Space Engineering

David Klerebladh

DEPARTMENT OF Microtechnology and Nanoscience
CHALMERS UNIVERSITY OF TECHNOLOGY
Gothenburg, Sweden 2025
www.chalmers.se

Master's thesis 2025

D-Band Transition from eWLB to Polymer Microwave Fiber:

Design, Fabrication, and Characterization

David Klerebladh

CHALMERS
UNIVERSITY OF TECHNOLOGY

Department of Microtechnology and Nanoscience
Division of Microwave Electronics
Millimeterwave/THz integrated circuits
Chalmers University of Technology
Gothenburg, Sweden 2025

D-Band Transition from eWLB to Polymer Microwave Fiber: Design, Fabrication, and Characterization
DAVID KLEREBLADH

Supervisor: Frida Strömbeck, Department of Microtechnology and Nanoscience
Supervisor: Parisa Aghdam, Ericsson AB
Examiner: Herbert Zirath, Department of Microtechnology and Nanoscience

Master's Thesis 2025
Department of Microtechnology and Nanoscience
Division of Microwave Electronics
Millimeterwave/THz integrated circuits
Chalmers University of Technology
SE-412 96 Gothenburg
Telephone +46 31 772 1000

Cover: Measurement setup, measurement results, simulation setup, and fabricated coupler mounted on eWLB package and PCB with the PMF connected.

Typeset in LaTeX
Printed by Chalmers Reproservice
Gothenburg, Sweden 2025

D-Band Transition from eWLB to Polymer Microwave Fiber: Design, Fabrication, and Characterization
DAVID KLEREBLADH
Department of Microtechnology and Nanoscience
Chalmers University of Technology

Abstract

This thesis investigates the design, fabrication, and characterization of coupling solutions between embedded Wafer-Level Ball Grid Array (eWLB) packages and Polymer Microwave Fibers (PMFs) for sub-terahertz communication, specifically targeting the 130–150 GHz portion of the D-band frequency range (110–170 GHz). PMFs offer significantly lower attenuation compared to free-space propagation, and better link efficiency and reach compared to copper solutions, as well as being more robust and cheaper compared to optical based solutions for short-range, high-data-rate applications. However, the current coupling solution—using an in-package Vivaldi antenna—suffers from high transition losses.

To address this, a dielectric coupling structure is proposed, designed to enhance electromagnetic field confinement and better match the modal profile of the PMF. The coupling system, including a back-to-back simulation setup, is modeled and optimized using the full-wave electromagnetic simulation tool High Frequency Structure Simulator (HFSS). The physical structure is fabricated using 3D printing in Acrylonitrile Butadiene Styrene (ABS), and its performance is verified through Vector Network Analyzer (VNA) measurements.

The measured results of the designed coupler show a coupling improvement over the 130-140 GHz frequency range of between 0.5-2.2 dB, compared to the previous solution. A maximum measured improvement of 2.2 dB is observed at 134 GHz. The designed coupler not only improves the coupling, but also gives a compact solution to hold the PMF in front of the eWLB package, and offers easy mounting on the Printed Circuit Board (PCB).

Keywords: eWLB package, PMF, Vivaldi antenna, D-band, dielectric waveguide, sub-THz communication, 3D-printing, coupling improvement, electromagnetic design.

Acknowledgements

This master thesis was carried out at Ericsson AB and at Chalmers University of Technology. First of all, I would like to thank Ericsson for funding this thesis project and Vinnova for partly funding it.
I would like to thank my supervisor at Ericsson, Parisa Aghdam, for all the help, encouragement, and support throughout this thesis. I also want to thank my supervisor at Chalmers, Frida Strömbeck, for her support, inputs, and help with all measurements along the way.
Thanks to Haojie Chang at Chalmers for answering many technical questions regarding the PCB, providing important design files, and for all the help with the measurements.
I am also grateful to Sining An from Ericsson for her supervision and for our discussions regarding measurements, and to Chantal Liao from Ericsson for both supervision and her great HFSS support. Thanks as well to Gilbert Johansson at Ericsson for taking care of the 3D-printing of the coupler designed in this work.
Finally, I want to thank the whole team at Ericsson Research and at Microwave Electronics at Chalmers for creating such a welcoming and inspiring environment. And a special thanks to all the other master thesis students at Ericsson — for making this a fun and memorable time.

David Klerebladh, Gothenburg, May, 2025

List of Acronyms

Below is the list of acronyms that have been used throughout this thesis listed in alphabetical order:

ABS	Acrylonitrile Butadiene Styrene
DU	Digital Unit
DWG	Dielectric Waveguide
eWLB	embedded Wafer-Level Ball Grid Array
HDPE	High-Density Polyethylene
HE	Hybrid Electric
HFSS	High Frequency Structure Simulator
LCP	Liquid Crystal Polymer
LDPE	Low-Density Polyethylene
MIMO	Multiple-Input Multiple-Output
MMIC	Monolithic Microwave Integrated Circuit
PCB	Printed Circuit Board
PEC	Perfect Electric Conductor
PE	Polyethylene
PIC	Photonic Integrated Circuit
PMF	Polymer Microwave Fiber
PS	Polystyrene
RDL	Redistribution Layer
RU	Radio Unit
TE	Transverse Electric
TEM	Transverse Electromagnetic
TM	Transverse Magnetic
UWB	Ultra-Wideband
VCSEL	Vertical-Cavity Surface-Emitting Laser
VNA	Vector Network Analyzer

Contents

List of Figures

List of Tables

1
Introduction

The 6GTandem project, which is an EU project that both Ericsson and Chalmers are part of, and to which this work is related, aims to develop a dual-frequency distributed Multiple-Input Multiple-Output (MIMO) system that utilizes both sub-10 GHz and sub-terahertz (sub-THz) frequency bands [1]. The sub-10 GHz band is primarily used for user localization, while the sub-THz band enables extremely high data rate transmission. As illustrated in Figure 1.1, the sub-THz Radio Units (RUs) are distributed along a Polymer Microwave Fiber (PMF), enabling efficient signal distribution in the system.

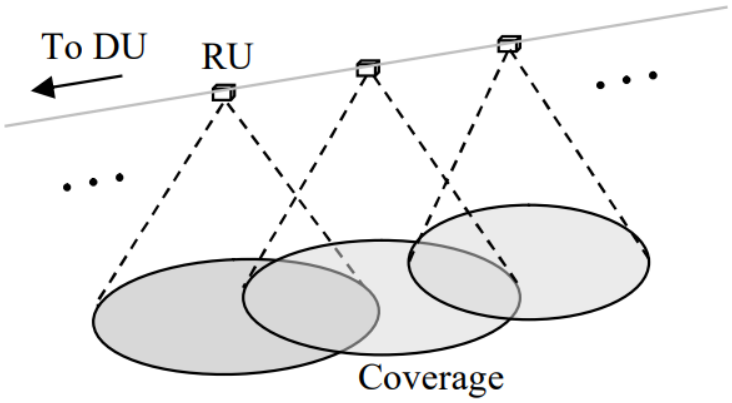

Figure 1.1: Distributed RUs along the PMF (from [2]).

Since the free-space path loss is huge at sub-THz frequencies, a promising solution to connect the RUs with the Digital Unit (DU), that both generate and process the signals, is using PMFs. At D-band frequencies (110-170GHz), as is considered in this work, they offer significantly lower attenuation compared to free-space propagation, and better link efficiency and reach in terms of energy per bit per meter compared to copper solutions, as well as being more robust and cheaper compared to optical Vertical-Cavity Surface-Emitting Laser (VCSEL) based solutions [3]. Figure 1.2 shows the link efficiency for different lengths of the different solutions.

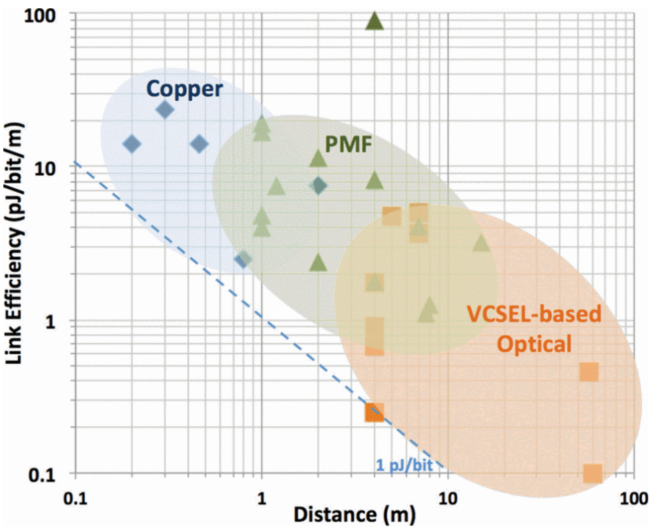

Figure 1.2: Link efficiency for different lengths for Copper, PMF and VCSEL based solutions (from [3]).

Figure 1.3 compares free-space path loss and PMF attenuation at 140 GHz. As seen in the figure, free-space path loss increases significantly with distance at short distances, whereas the PMF exhibits a linear increase in attenuation. The figure provides an estimate of the distance at which PMF becomes advantageous compared to free-space propagation. However, the figure does not account for antenna gains in free-space transmission, which can significantly impact the overall link budget and extend the practical range of free-space communication.

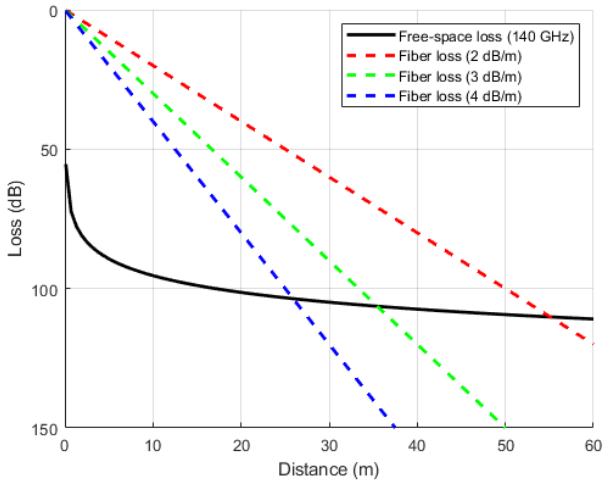

Figure 1.3: Free-space loss at 140 GHz and PMF with an attenuation of 2,3, and 4 dB per meter.

At the RUs, a packaging technique called embedded Wafer-Level Ball Grid Array (eWLB)—a proprietary technology developed by Infineon—is used [4]. This packaging approach enables the integration of components such as the Monolithic Microwave Integrated Circuits (MMICs), the transmit and receive antennas, and the

coupling antenna used to interface with the PMFs. The eWLB package is mounted onto the Printed Circuit Board (PCB) via solder balls which provides interconnects for biasing.

1.1 Motivation

The current coupling solution between the eWLB and the PMF within 6GTandem, with the avaiable hardware, constists of a Vivaldi antenna in the eWLB package, coupling the signal into the PMF, however, this solution suffers from around 4 dB of loss per transition. Meaning that for each RU, there will be around 8 dB of coupling losses.
The aim of this work is to design a structure that is added around the eWLB, to help couple the signal towards the PMF. The idea is that the already fabricated packages can be used, and that the designed coupler from this work will eventually improve the performance, and hold the PMF in front of the eWLB.

1.2 Prior work

To better understand existing methods for coupling signals between PMFs and integrated circuits or PCBs, a literature study was conducted. The review identified several coupling strategies, which vary depending on the antenna type and system requirements. Broadly, these techniques can be classified as either lateral coupling, where the PMF is placed above the antenna in the same plane, and frontal coupling, where the PMF is aligned directly in front of the antenna aperture [3]. The choice of coupling topology is typically influenced by radiation characteristics of the coupling antenna and system integration constraints. Several works using these approaches are summarized below.

A planar transition from a 1 mm coaxial connector to a Polystyrene (PS) rectangular Dielectric Waveguide (DWG) was developed in [5] for W-band frequencies. The transition uses a microstrip-to-slotline conversion on a Liquid Crystal Polymer (LCP) substrate, followed by a slotline-fed tapered DWG. The structure achieved an insertion loss of approximately 2 dB per transition over the 50–85 GHz range.

Another relevant study is presented in [6], where a broadband microstrip line to DWG transition was developed for dual-polarized applications at W-band frequencies. The transition is based on a stacked-patch topology, where a primary microstrip-fed patch excites a secondary parasitic patch mounted inside a circular DWG made of High-Density Polyethylene (HDPE). This design enables broadband excitation of both orthogonal polarizations (HE_{11}-x and HE_{11}-y) with low complexity and minimal space requirements. To further enhance coupling, a dielectric stamp was included at the bottom of the DWG. Measurements showed an insertion loss below 1.8 dB across bandwidth from 80–90 GHz, with a minimum insertion loss of 1.2 dB at 83 GHz.

A study by Hassona et al. [7] presents a D-band waveguide-to-microstrip transition implemented using eWLB packaging technology. A patch radiator integrated into the Redistribution Layer (RDL) of the eWLB couples the signal to a D-band rectangular waveguide. The transition demonstrated a measured insertion loss of 2.1 dB over a 26 GHz bandwidth, showing competitive performance with a compact and highly integrated packaging solution.

One example of more recent work is presented in [8], where a D-band data link based on a PMF was developed. The system consisted of a SiGe HBT-based transceiver MMIC wire-bonded to a PCB, with electromagnetic coupling into the PMF achieved via an on-board Franklin antenna launcher. The transition between the MMIC and the PMF was characterized by an insertion loss of approximately 5–5.5 dB across 135–155 GHz. In this work, the PMF featured a rectangular solid core, with the core extending above the PCB surface, allowing the Franklin antenna to provide lateral coupling into the PMF.

Most closely related to the work in this thesis is the recent study presented in [9], where a PMF coupler integrated into an eWLB package was developed for sub-THz communication at around 140 GHz. In this work, a single-layer antipodal Vivaldi antenna was designed in the redistribution layer of the eWLB to laterally excite the fundamental modes of a solid rectangular PMF. The coupling performance achieved a measured coupling loss of approximately 4 dB at 140 GHz.

Table 1.1 shows a comparison of the different coupling solutions mentioned above and their performance.

Table 1.1: Summary of coupling methods for PMF and DWG transitions

Year	**Method**	**Frequency Range**	**Coupling Loss**
2016	Microstrip-to-slotline transition to tapered DWG [5]	50–85 GHz	∼2 dB
2019	Stacked-patch microstrip line to circular DWG [6]	80–90 GHz	1.2–1.8 dB
2020	Patch radiator in eWLB to D-band rectangular waveguide [7]	122–148 GHz	2.1 dB
2024	Franklin antenna launcher on PCB to rectangular PMF [8]	135–155 GHz	∼5–5.5 dB
2024	Single-layer antipodal Vivaldi antenna in eWLB package to rectangular PMF [9]	∼140 GHz	∼4 dB

1.3 Evaluation of coupling solutions

This work focuses on improving the coupling between a Vivaldi antenna integrated into the RDL of an eWLB package and a PMF. At the beginning, several alternative approaches were explored to enhance the electromagnetic field transfer from the in-package antenna to the PMF.
Among the investigated concepts were the use of a reflecting metasurface placed above the antenna to redirect upward-leaking energy toward the PMF, and a graded-index (GRIN) lens that could be positioned above or in front of the antenna to guide the field smoothly into the PMF.
While these approaches showed potential, they also introduced additional design complexity and would have required more time to optimize, fabricate, and integrate into the system. Given the scope and time constraints of a master's thesis project, a more practical solution was chosen.
The final coupler design investigated in this work is a dielectric coupling structure placed above and in front of the eWLB package. This configuration was selected for its simplicity, ease of prototyping, and ability to enhance coupling efficiency by shaping the electromagnetic field toward the PMF. Early simulation results showed promising performance, making it a candidate for further development and fabrication.

2
Theory

This section introduces the theory of electromagnetic wave propagation through various waveguides and transmission lines, antenna theory, as well as packing techniques for MMICs and antennas.

2.1 Transmission lines and waveguides

To guide high-frequency signals on a PCB or MMIC, we need transmission lines. Classical circuit theory is not applicable when the lengths of the conductors are comparable with the wavelength of the signal, since the voltage cannot be assumed to be the same throughout the conductor. For these high frequencies, a new circuit theory is needed, taking into account the dimensions and characteristics of the transmission line, as well as how the power is propagating through it [10].
However, as the frequency increases even further, in the millimeter-wave and terahertz ranges, transmission line losses such as conductor and dielectric losses become very large. At these frequencies, traditional planar transmission lines exhibit high attenuation and radiation, which limits their performance over longer distances.
To overcome these limitations, waveguides are used. Waveguides provide a low-loss medium for guiding high-frequency electromagnetic waves, particularly in the microwave and millimeter wave regions. Unlike transmission lines, which rely on current flow through conductors, waveguides confine and guide waves through boundary conditions which support different propagation modes of the electromagnetic wave. Their closed or semi-closed metallic or dielectric structures ensure minimal radiation - leading to low attenuation and better power-handling capability, making them ideal for applications requiring high efficiency, isolation, and bandwidth [10].

2.1.1 General transmission line theory

Transmission lines are essential components in high-frequency circuits, responsible for guiding electromagnetic waves with minimal loss and distortion. They enable efficient signal propagation while maintaining impedance matching to avoid reflections. Different types of transmission lines are used depending on the application, frequency range, and manufacturing limitations.

2.1.2 Mircrostrip line

A microstrip line consists of a conducting strip placed on a dielectric substrate with a ground plane on the opposite side. It is widely used in microwave circuits because

of simple fabrication and integration with PCBs and MMICs. The microstrip line supports the so-called quasi-Transverse Electromagnetic mode (quasi-TEM), which is a special case of the classical TEM mode, where the field is within two different media. Based on this, an empirical model describing the effective permittivity of a single dielectric, ϵ_e, surrounding the conductor is obtained, as well as the characteristic impedance, Z_0, of the line [10].

$$\epsilon_e = \frac{\epsilon_r + 1}{2} + \frac{\epsilon_r - 1}{2} \frac{1}{\sqrt{1 + 12d/W}} \tag{2.1}$$

$$Z_0 = \begin{cases} \frac{60}{\sqrt{\varepsilon_r}} \ln\left(\frac{8d}{W} + \frac{W}{4d}\right), & \text{for } \frac{W}{d} \leq 1 \\ \frac{120\pi}{\sqrt{\varepsilon_e}} \left[\frac{W}{d} + 1.393 + 0.667 \ln\left(\frac{W}{d} + 1.444\right)\right]^{-1} & \text{for } \frac{W}{d} \geq 1 \end{cases} \tag{2.2}$$

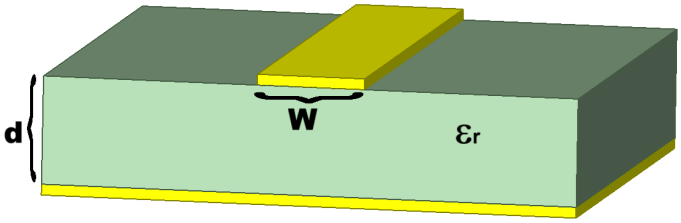

Figure 2.1: A microstrip line model, with the conductor and ground plane in yellow and the dielectric substrate in green.

2.1.3 Strip line

A strip line is a fully enclosed transmission line where the conducting strip is embedded between two parallel ground planes within a dielectric substrate. This configuration provides better shielding and reduced radiation losses compared to microstrip lines, making it suitable for high-frequency applications where signal integrity is critical. The propagating mode of the strip line is a TEM and all of the field is confined in the dielectric around the strip and the two ground planes. Based on the width of the strip, and the thickness of the dielectric, an effective width of the strip, W_e, can be calculated, as well as the characteristic impedance of the strip [10].

$$\frac{W_e}{b} = \frac{W}{b} - \begin{cases} 0 & \text{for } \frac{W}{b} > 0.35 \\ (0.35 - W/b)^2 & \text{for } \frac{W}{b} < 0.35 \end{cases} \tag{2.3}$$

$$Z_0 = \frac{30\pi}{\sqrt{\epsilon_r}} \frac{b}{W_e + 0.441b} \tag{2.4}$$

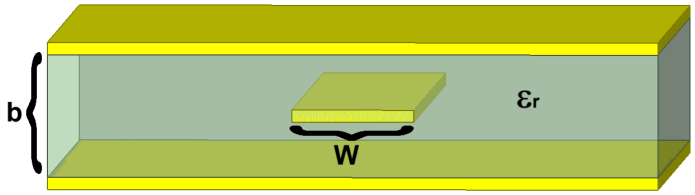

Figure 2.2: A strip line model, with the conductor and ground plane in yellow and dielectric substrate in light green

2.1.4 Slot line

A slot line consists of a narrow slot cut into a ground plane. Unlike microstrip and strip line, which use metallic conductors, slot lines rely on the dielectric substrate for wave propagation. They are commonly used in high-frequency circuits due to their capability to support unbalanced signals, easy fabrication and integration with other components.
As with microstrip lines, the impedance of slot lines has been characterized through measurements, as described in [18]. However, this analysis is limited to geometries where the gap-to-substrate ratio falls within $0.02 \leq \mathrm{W/d} \leq 1$.

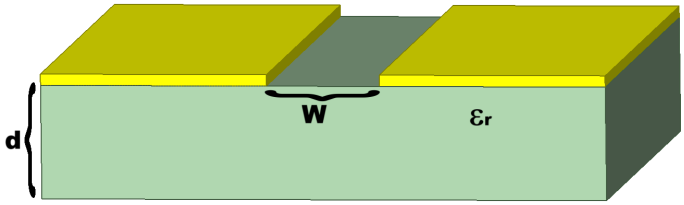

Figure 2.3: A slot line model, with the conductors in yellow and the dielectric substrate in green

2.1.5 General waveguide theory

Waveguides are structures designed to confine and direct electromagnetic waves, enabling efficient energy transmission with minimal loss. Unlike transmission lines, which rely on conductive paths, waveguides guide waves through controlled boundary conditions, supporting various propagation modes depending on their geometry and material properties.

2.1.6 Metallic waveguides

Metallic waveguides, such as rectangular and circular waveguides, are hollow conductive structures that confine electromagnetic waves through total internal reflection at the metallic boundaries. These waveguides primarily support Transverse Electric (TE) and Transverse Tagnetic (TM) modes, as TEM waves cannot propagate in

hollow waveguides. They are widely used in microwave and millimeter-wave applications due to their low loss and high power-handling capability. The impedance of the waveguide is defined depending on the mode of propagation. In this case we study the TE mode, which include the fundamental mode of the rectangular waveguide, TE_{10}, which has the lowest cutoff frequency. But, any TE_{mn} mode's cutoff frequency can be calculated and used. A standard dimensioning of a rectangular waveguide is a = 2b, and a = $\frac{c}{2f_{10}}$, where f_{10} is the cutoff frequency, f_c, of the TE_{10} mode [10].

$$Z_{TE} = \frac{k\eta}{\beta} \tag{2.5}$$

$$\beta = \sqrt{k^2 - k_c^2}, \quad k = \omega\sqrt{\mu\varepsilon}, \quad k_c = \sqrt{\left(\frac{m\pi}{a}\right)^2 + \left(\frac{n\pi}{b}\right)^2} \tag{2.6}$$

$$f_c = \frac{c}{2\pi\sqrt{\varepsilon_r}}\sqrt{\left(\frac{m\pi}{a}\right)^2 + \left(\frac{n\pi}{b}\right)^2} \tag{2.7}$$

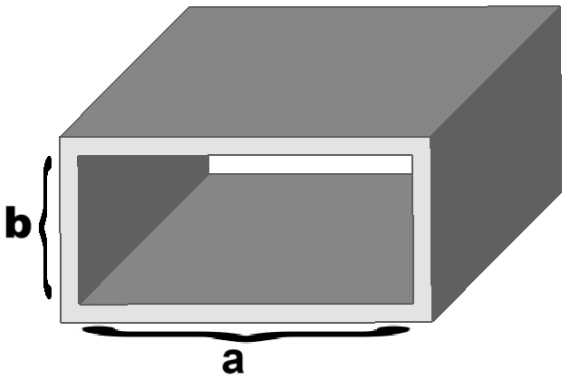

Figure 2.4: A rectangular waveguide model, with the metallic boundary in gray and the hollow air section in the middle as transparent.

Similarly, as with rectangular waveguides, the circular waveguides do not support the TEM mode. The fundamental mode of the circular waveguide is the TE_{11} mode. The impedance and cutoff frequency are described in [10].

2.1.7 Optical fibers

Optical fibers are dielectric waveguides that guide light through total internal reflection between a high-refractive-index core and a lower-refractive-index cladding. They support single-mode or multimode propagation, depending on the core diameter and wavelength of operation. Optical fibers are the backbone of modern communication networks, offering low-loss, high-bandwidth transmission for long-distance data communication [11].

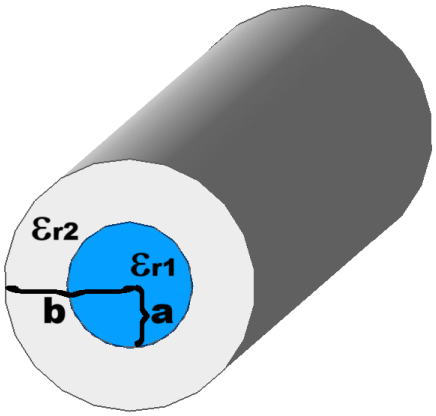

Figure 2.5: An optical fiber model, with the core in blue and the cladding in gray.

2.1.8 Dielectric waveguides and PMFs

DWGs consist entirely of non-metallic materials and guide electromagnetic waves using refractive index contrasts rather than metallic boundaries. These structures are used in millimeter-wave circuit interconnects, Photonic Integrated Circuits (PICs), and THz communication systems due to their ability to support low-loss propagation at high frequencies. DWGs can be both solid and hollow, and they can have a more complex geometry with a core dielectric, which itself can have a hollow section in the middle, and then a cladding with a lower permitivitty dielectric surrounding the core, similar to an optical fiber. These types of DWGs are often called PMFs. These PMFs can have rectangular, circular, or elliptical cores, which can be both solid or hollow, usually with a circular cladding surrounding them [12]. The PMF used in this work has a circular hollow core as in Figure 2.6.

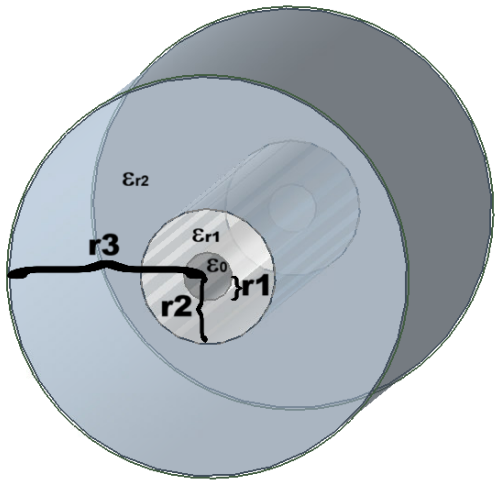

Figure 2.6: A PMF model, with the hollow section as transparent (ϵ_0), the core as silver (ϵ_{r1}), and the cladding as gray (ϵ_{r2}).

2.2 General antenna theory

An antenna is a physical structure that enables the transmission and reception of electromagnetic waves. It couples guided waves in transmission lines and waveguide to free-space radiation, for the transmitting case, and the other way around for the receiving case. Antennas are fundamental components in telecommunications, radar, satellite communication, and radio astronomy.
There exists a wide variety of antenna types, each optimized for specific applications and frequency ranges. Common examples include microstrip antennas, slot antennas, horn antennas, and reflector antennas.
In addition to single-element designs, antennas can be configured into arrays, where multiple elements are spatially arranged and fed in a controlled manner. Antenna arrays enable increased gain, beam steering, beam shaping, making them essential in modern systems like 5G base stations and phased-array radars [13].

2.2.1 Radiation and field regions

If we observe a field at a large distance, r, away from the antenna, where r is given

$$r \geq 2D^2/\lambda \tag{2.8}$$

, and D is the size of the antenna in its largest dimension, we are in the far-field region. In the far-field region, the field variations with distance, r, and direction, $\hat{r}$, become separable, and are described by the far-field function in Equation 2.9.

$$\mathbf{E(r)} = G(\hat{r})e^{-jkr}/r \tag{2.9}$$

In this case, only from a measure of the directional dependence, $G(\hat{r})$, of the amplitude and phase of the field, can the field be reconstructed, at any point in the far-field.
For distances smaller than $2D^2/\lambda$, we are in the near-field region. At the very closest to the antenna, we are in the reactive near-field region, which means that non-radiating, and reactive oscillating power dominates. The field in this region cannot be defined in general because it is heavily dependent on the antenna geometry. In the near-field, as we approach the far-field distance, we are in the so-called radiating near-field region. Typically, this region starts 2-3λ away from the antenna, as the reactive effects disappear [13].

2.2.2 Directivity and gain

The directive gain is an important concept when speaking about antenna characteristics. It describes how much an antenna is radiating in a certain direction, in relation to an isotropic antenna, meaning that it radiates an equal amount in all directions. The directive gain has a unit of dBi, which is dB in relation to the isotropic level.
The maximum directive gain of an antenna, is called the directivity, **D**. This is the center point of the main beam direction, i.e the direction where most of the power is radiated.

The gain of an antenna, **G**, is taking into account both the directivity and the antenna efficiency, η.

$$\mathbf{G} = \eta\mathbf{D} \tag{2.10}$$

The antenna efficiency is taking into account both impedance missmatch at the input port, conductive- and dielectric losses, aperture efficiency, and polarization efficiency [13].

2.2.3 Field patterns

The field pattern of an antenna describes how the strength of the radiated electromagnetic field varies with direction in space. It is typically represented in terms of the electric field magnitude and visualized using polar or rectangular plots.
For linearly polarized antennas, two important cuts are often investigated. The E-plane, which is the plane containing the electric field vector and the direction of maximum radiation, and the H-plane, which contains the magnetic field vector and the direction of maximum radiation.
Depending on the type of antenna, the main beam can be directed along different orientations. In broadside antennas, such as microstrip patches, the maximum radiation is perpendicular to the plane of the antenna. In contrast, endfire antennas, like a tapered slot antenna, radiate along the axis of the antenna structure [13].

2.3 Vivaldi antenna

Vivaldi antennas are a class of tapered slot antennas known for their broadband performance and high directivity. They operate based on the principle of traveling-wave radiation, where an electromagnetic wave gradually transitions from a guided mode to free-space propagation through an exponentially flared slot. These antennas are widely used in radar systems, Ultra-Wideband (UWB) communications, and high-frequency imaging applications due to their ability to cover a broad frequency range with stable radiation characteristics [14].
The overall dimensions of a Vivaldi antenna are typically expressed in terms of the free-space wavelength, λ_0, at the lowest operating frequency of the design. The length of the tapered section, L, is typically chosen to be around $2\lambda_0$, while the final aperture width, W, is often designed to be approximately $0.5\lambda_0$. The dielectric substrate thickness, h, is kept much smaller than the wavelength (e.g., $h \approx \lambda_0/20$) to maintain good impedance control and to suppress surface wave propagation.
The flare profile of the exponentially tapered slot follows the equation [15]:

$$y(x) = ae^{bx} + c, \tag{2.11}$$

where the parameters a, b, and c are selected to define the desired flare shape. These values are typically chosen to match the feed lines at the input and to achieve a smooth impedance transition toward the aperture at the end of the taper.
Based on classical traveling-wave antenna theory, the performance of endfire antennas like the Vivaldi can be estimated using approximate design rules [15]. For a

physical taper length L, the directivity is given by:

$$D \approx 10 \log_{10} \left(10 \frac{L}{\lambda_0} \right) \quad [\text{dB}] \tag{2.12}$$

with a corresponding beamwidth of:

$$\text{BW} \approx \frac{55^\circ}{\sqrt{L/\lambda_0}}. \tag{2.13}$$

If lower sidelobes and broader bandwidth are prioritized, the trade-off is a slightly reduced directivity:

$$D_{\text{low-sidelobe}} \approx 10 \log_{10} \left(4 \frac{L}{\lambda_0} \right), \tag{2.14}$$

with a broader beamwidth of:

$$\text{BW}_{\text{broadband}} \approx \frac{77^\circ}{\sqrt{L/\lambda_0}}. \tag{2.15}$$

2.3.1 Standard Vivaldi antenna

The standard Vivaldi antenna consists of a single-sided exponentially tapered slot on a dielectric substrate. This design offers broad bandwidth and high gain while maintaining a relatively simple planar structure, making it suitable for printed circuit implementations [16].

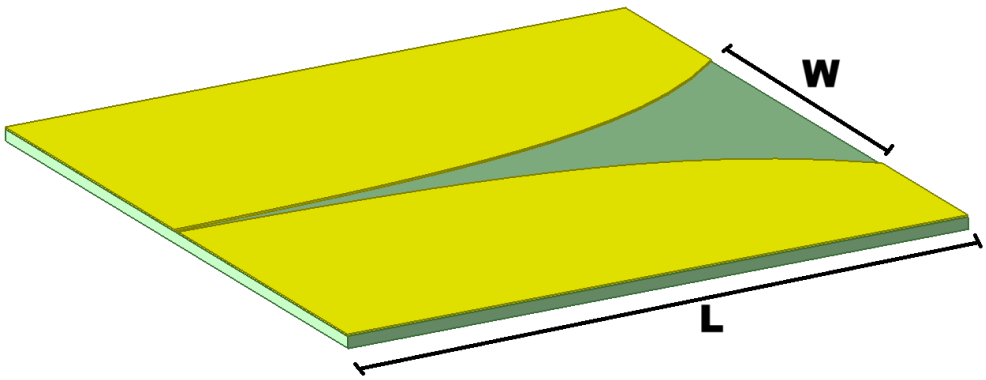

Figure 2.7: A standard vivaldi antenna model, with the conductors in yellow, and dielectric substrate in green.

2.3.2 Antipodal Vivaldi antenna

The antipodal Vivaldi antenna features two conductive flares positioned on opposite sides of the dielectric substrate. This design allows for improved impedance matching and a more balanced current distribution, leading to better radiation efficiency

and reduced cross-polarization. The top flare can be seen as the conductor, while the bottom flare can be seen as the ground [17].

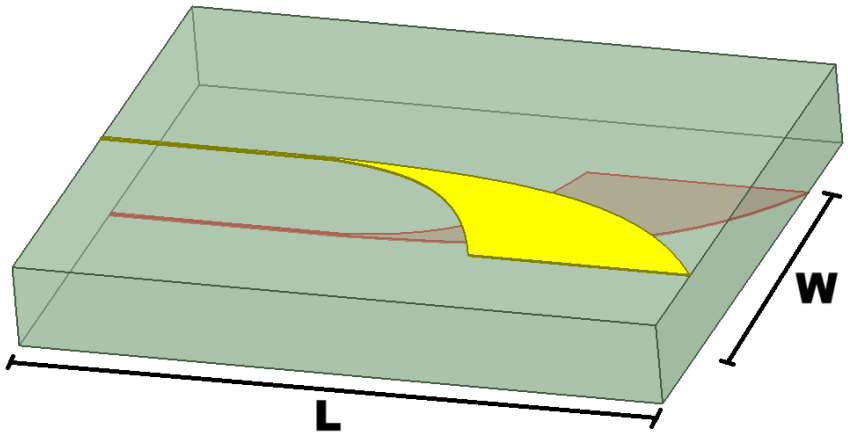

Figure 2.8: An antipodal Vivaldi antenna model, with the conductor flare in yellow, ground flare in red, and the dielectric substrate in green.

2.3.3 Gain enhancement of Vivaldi antennas

To improve the radiation characteristics of Vivaldi antennas—corrugation is a widely used technique. Corrugation refers to periodic, evenly spaced slots introduced along the outer edges of the flared sections of the antenna. These modifications enhance antenna parameters such as gain, and return loss.
Corrugations suppress surface waves and reduce sidelobes, thereby focusing more energy in the desired endfire direction. Different geometries such as sine-shaped, rectangular, triangular, and slanted corrugations have been explored in literature [17]. Rectangular corrugations with decreasing slot size towards the aperture have been demonstrated to deliver high gain while minimizing return loss.
By appropriately choosing the corrugation type and size, significant improvements can be made to the antenna's overall performance without increasing its physical footprint or fabrication complexity. Figure 2.9 shows the difference in geometry between a standard Vivaldi antenna and one enhanced with corrugations applied along the outer taper edges.

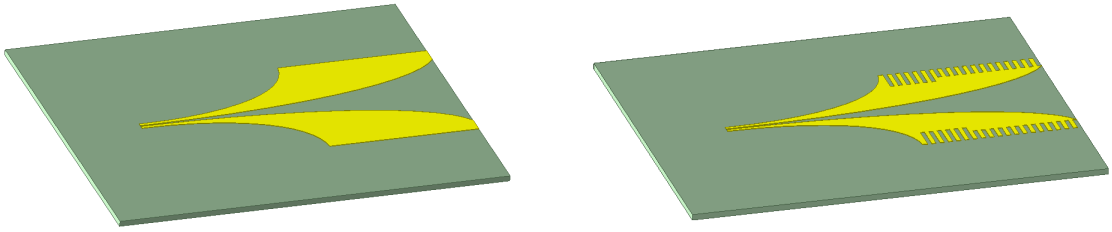

(a) A Vivaldi antenna model without corrugations. The conductor is shown in yellow, and the dielectric in green.

(b) A Corrugated Vivaldi antenna model. The conductor is shown in yellow, and the dielectric in green.

Figure 2.9: A comparison of Vivaldi antenna geometries: (a) standard and (b) corrugated.

Figure 2.10 illustrates the effect of corrugations on the radiation patterns of a Vivaldi antenna. As seen in (b), the E-plane radiation exhibits a stronger and narrower main lobe compared to the uncorrugated version in (a), indicating enhanced directivity due to corrugation. The maximum gain (towards $\theta = 90°$), in the E-plane, for the uncorrugated case is 7.7 dB, and for the corrugated case it is 8.7 dB. This aligns with the theoretical role of corrugations, which guide the electromagnetic wave more effectively toward the aperture by suppressing surface waves.
In addition to the improvement in the E-plane, the H-plane radiation is also noticeably affected. The corrugated antenna shows a significantly weaker H-plane radiation level, with a maximum gain of -8.7 dB (towards $\theta = 90°$), compared with -4.2 dB for the uncorrugated, suggesting that the corrugations help confine the radiated energy more efficiently in the E-plane direction. This leads to better endfire performance and reduced lateral spreading of the beam.

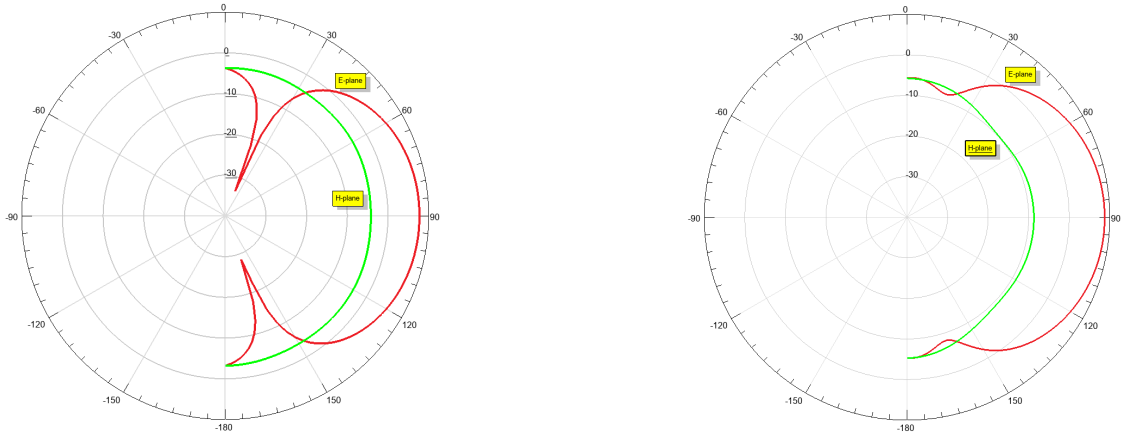

(a) Radiation pattern of an uncorrugated Vivaldi antenna.

(b) Radiation pattern of a corrugated Vivaldi antenna.

Figure 2.10: Radiation pattern comparison of Vivaldi antennas: (a) uncorrugated and (b) corrugated.

2.4 eWLB package

The eWLB package, which is a proprietary technology developed by Infineon, is a modern packaging technology well-suited for millimeter-wave systems due to its compact size, low parasitics, and excellent RF performance [4]. Unlike traditional packaging approaches, eWLB allows redistribution of interconnects beyond the chip boundaries, enabling the integration of antennas, transmission lines, and passive components directly within the package itself.
At the core of eWLB technology is the thin-film Redistribution Layer (RDL), which serves as an interconnection medium between the MMIC and other components, such as antennas. For mm-wave frequencies, the RDL offers low-loss signal paths with precisely controlled impedance and minimal parasitic effects. Typical transmission lines used in the RDL include coplanar waveguides and coplanar strip lines, exhibiting attenuations as low as 0.12–0.46 dB/mm at 77 GHz [4].
In this work, a Vivaldi antenna is integrated directly into the RDL layer. This antenna is connected to the MMIC through short interconnects within the package, ensuring efficient signal transition and minimizing reflection losses. The integration in the RDL enables the antenna to benefit from the low-loss, high-resolution metal patterning capabilities of the eWLB process, and it eliminates the need for lossy transitions to the PCB at mm-wave frequencies.

3

Modeling and simulations

This chapter presents the design and integration of the PMF coupling system. It begins with the electromagnetic modeling of the PMF itself, where both modal properties and attenuation are analyzed and validated through measurements. The chapter then proceeds with the design and simulation of the Vivaldi antenna, its integration into the eWLB package, and the modeling of the multilayer PCB used to support the package. Finally, the complete coupling setup is assembled—including the PMF in front of the antenna—and a back-to-back simulation environment is introduced to characterize the overall coupling performance.

3.1 PMF modeling

This work considers a circular hollow PMF developed by HUBER+SUHNER, featuring a core made of Polyethylene (PE) and a cladding made of Low-Density Polyethylene (LDPE) foam. The core has a dielectric constant (D_k) of 2.3 and dielectric loss tangent ($\tan(\delta)$) of 30e-5, while the cladding has D_k equal to 1.3 and $\tan(\delta)$ equal to 13e-5. Figure 3.1 shows a sketch of the PMF's cross-section. An image of the PMF is shown in Figure 3.2.

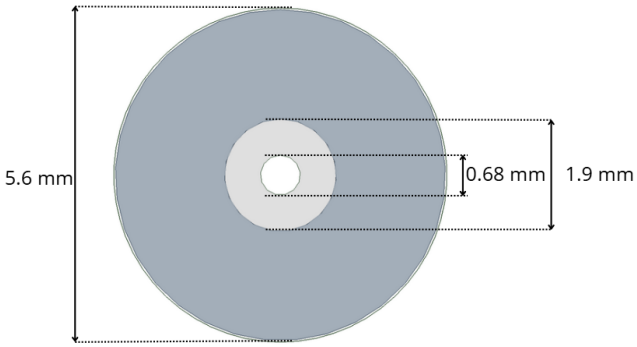

Figure 3.1: Dimensions of the circular hollow PMF.

(a) Cross-section of the PMF. (b) Side view of the PMF.

Figure 3.2: Illustration of the PMF: (a) Cross-section view and (b) Side view.

Full-wave electromagnetic simulations of the PMF were performed using Ansys HFSS. It was modeled with its physical geometry and material properties to analyze its wave propagation characteristics. The simulation enabled accurate extraction of attenuation and group delay across the D-band frequency range.
In Figure 3.3, the simulation setup is shown. The PMF is excited using a modal wave port to analyze the different propagating modes. The wave ports are backed by cylindrical Perfect Electric Conductors (PECs) to confine the fields and prevent unwanted back radiation, ensuring accurate mode excitation. The PMF is surrounded by a radiation boundary to represent free-space and allow energy to leave the simulation domain without reflection.

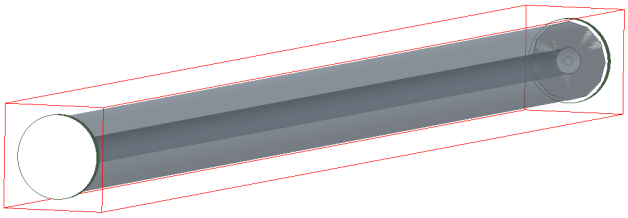

Figure 3.3: Simulation setup of the PMF in HFSS.

From this setup, the five lowest-order excited modes were analyzed. In Figure 3.4, the imaginary part of the propagation constant - being the phase constant β, is plotted over the full D-band frequency range. The plot shows that the propagating modes in the PMF are all propagating in D-band. Mode 1 and mode 2 have the same propagation characteristics - indicating that the fundamental mode is degenerate and that what is refered to mode 1 and mode 2, are in fact two different polarizations of the fundamental Hybrid Electric (HE_{11}) mode.

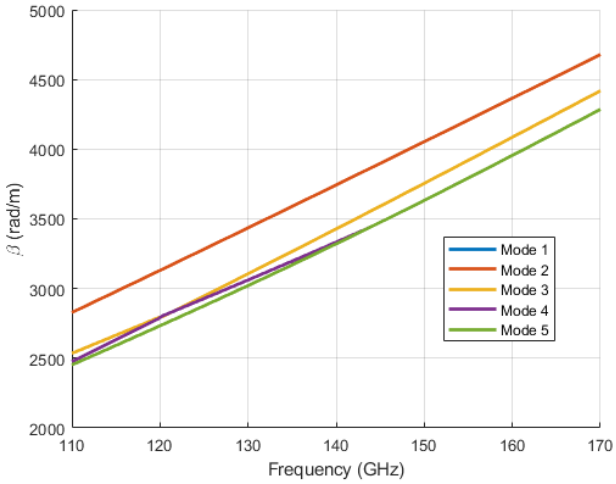

Figure 3.4: The phase constant of the first five propagating modes in the PMF.

These modes are further investigated by observing their attenuation. The attenuation of the first five modes are plotted in Figure 3.5(a), and the attenuation of the two different polarizations of the fundamental mode, are also included for clarity in Figure 3.5(b). Figure 3.5(a) shows that modes 3, 4, and 5 are heavily attenuated.

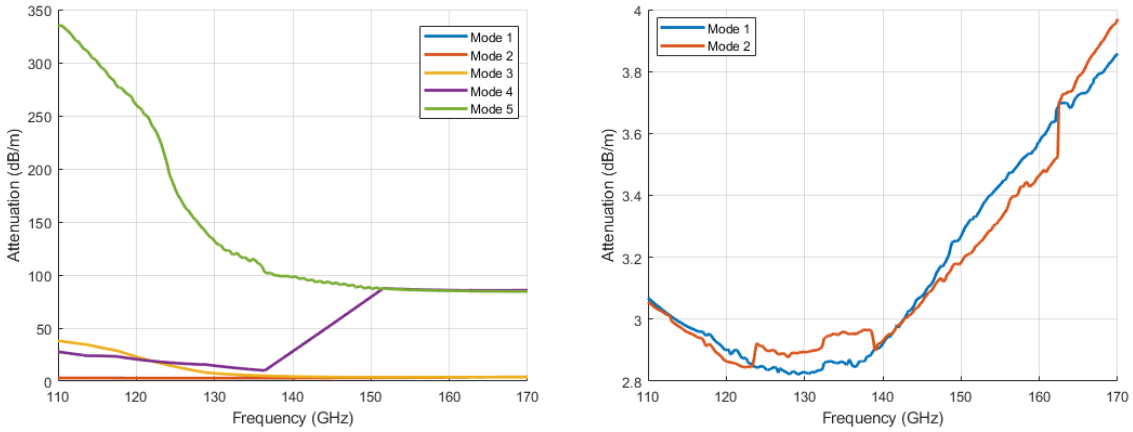

(a) Attenuation of the first five propagating modes in the PMF.

(b) Attenuation of the first two propagating modes in the PMF.

Figure 3.5: Attenuation characteristics of the propagating modes in the PMF: (a) the five lowest-order modes, and (b) the two dominant modes.

The field distribution of the fundamental mode, is shown in Figure 3.6. The electric field magnitude at the cross-section of the two polarizations are the same. The difference between them is observed when looking at the electric field vector, showing the difference in polarization in Figure 3.7.

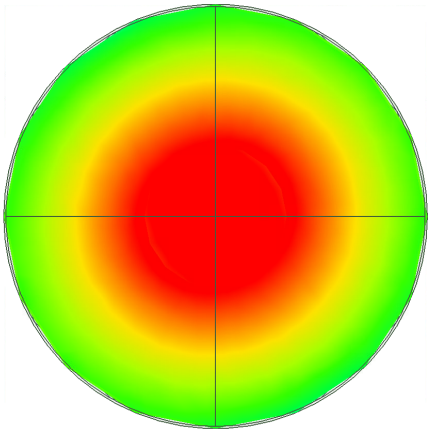

Figure 3.6: Cross-sectional electric field magnitude in the PMF at 140 GHz

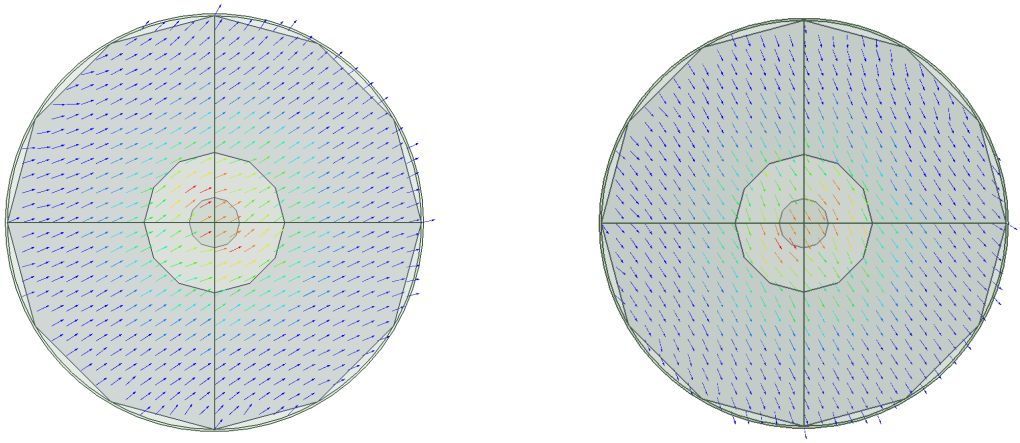

(a) HE_{11} mode with horizontal polarization.

(b) HE_{11} mode with vertical polarization.

Figure 3.7: Polarization of the HE_{11}: (a) Horizontal (b) Vertical.

To validate the simulation of the modeled PMF, measurements were performed on PMFs of four different lengths, being 1, 2, 4, and 8 meters. The goal was to extract the attenuation and group delay of the PMF to compare that with simulations.
A Vector Network Analyzer (VNA) with D-band frequency extenders was used to perform the measurements in the 110–170 GHz range. The frequency extender features a rectangular waveguide output port, which was connected to a rectangular-to-circular waveguide transition. Following this, a circular waveguide-to-PMF transition developed by HUBER+SUHNER was used to efficiently launch the fundamental HE_{11} mode into the PMF. The measurement setup can be seen in Figure 3.8.

Figure 3.8: PMF measurement setup.

Since the connector and transition losses remain constant regardless of PMF length, their contribution was de-embedded by analyzing the differences between measurements of varying lengths. Observing how the transmission magnitude and phase delay scale with length, the PMF attenuation and group delay was extracted. The measured and simulated attenuation are plotted in Figure 3.9(a), and the measured and simulated group delay are plotted in Figure 3.9(b).

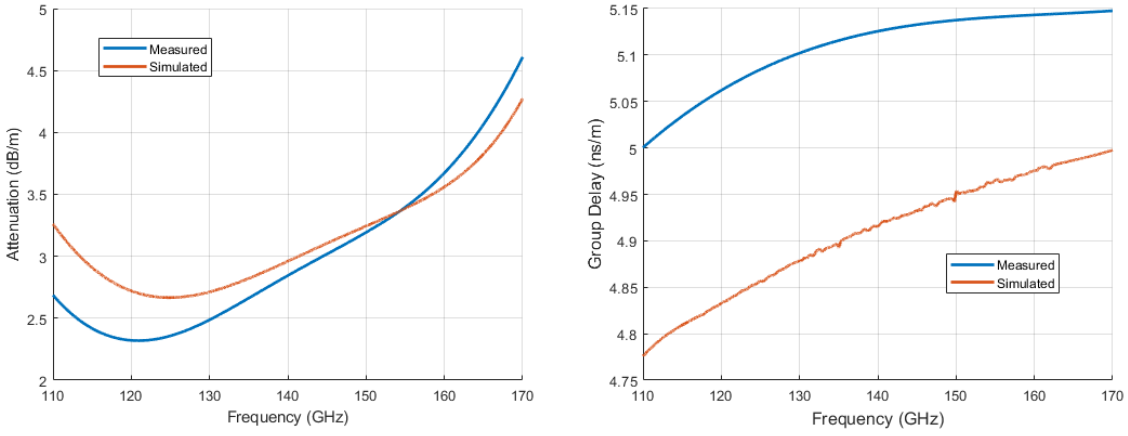

(a) Measured and simulated attenuation of the PMF.

(b) Measured and simulated group delay of the PMF.

Figure 3.9: Comparison of measurement and simulation: (a) Attenuation and (b) Group delay of the PMF.

3.2 eWLB modeling

The design and simulation of the integrated Vivaldi antenna began with a layout file containing the physical geometry of the antenna. This layout defined the shape of the antenna and the feed region, and served as the foundation for electromagnetic simulations. The geometry was imported into HFSS and the thickness was set to match the thickness of the RDL. Figure 3.10 shows the layout of the Vivaldi antenna used in this work.

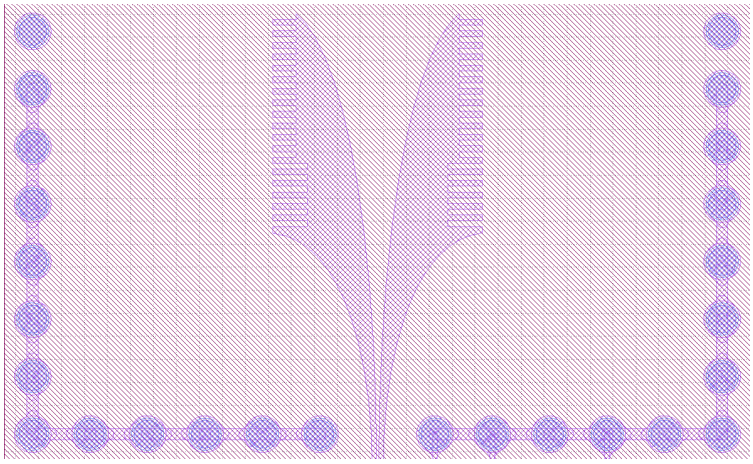

Figure 3.10: Layout view of the Vivaldi antenna.

In addition to the antenna layout, a detailed 3D model of the eWLB package was provided as an HFSS project file. The model included realistic structural details such as the RDL, mold compound, and the backside protection layer, allowing for accurate simulation of electromagnetic interactions within the package. Adjustments were made to the package to match the size of the specific package used in this work, as well as to add connections to the solder balls. The Vivaldi antenna layout was then integrated into the eWLB package, positioned within the RDL. This enabled full-wave simulation of the antenna's performance in the package. Figure 3.11 shows the integrated antenna inside the eWLB model.

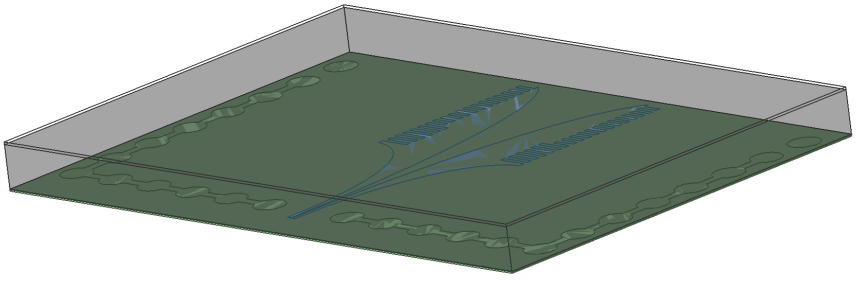

Figure 3.11: Vivaldi antenna embedded in the RDL layer of the eWLB package.

3.3 eWLB on PCB modeling

The design of the PCB hosting the eWLB package was also based on an initial layout file. This file contained the metallization patterns, ground planes, and mechanical cutouts used to mount and connect the package. The PCB used is made by MULTEK and offers six signaling layers, four prepreg layers being Megatron Prepreg R-5680(N), and one core laminate layer being Megatron laminate (R-5785(N). Figure 3.12 shows the layout view of the part of the PCB on which the eWLB coupler is mounted. The circles show the vias, and the large rectangle in the middle shows the part of the PCB where the ground plane is removed. In this part, there is only dielectric, forming a cavity underneath the eWLB package. The vias are used for interconnects between the eWLB package and the PCB, as well as providing isolation from the coupling antenna.

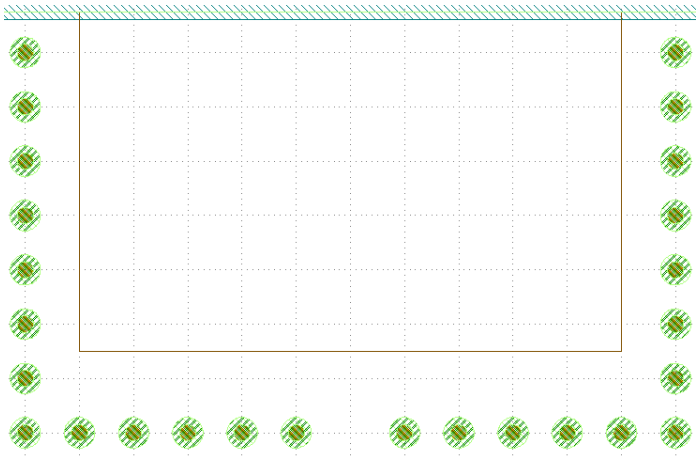

Figure 3.12: Layout view of the PCB, showing signal lines and package pad geometry.

Using the layout as a reference, a full 3D model of the PCB was constructed in HFSS. The model includes the dielectric substrates, copper layers, vias, and solder pads. Figure 3.13 shows the HFSS model of the PCB.

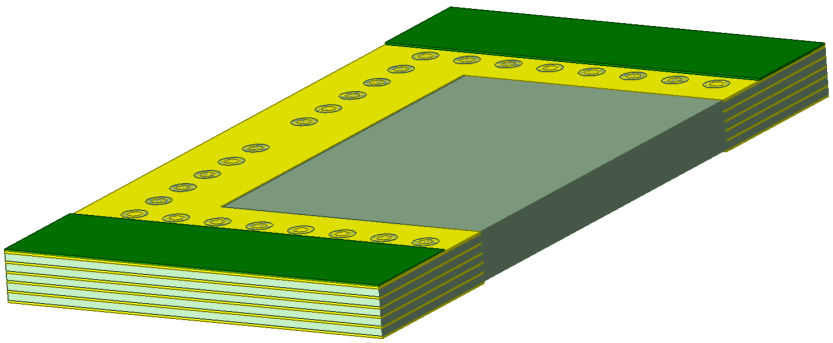

Figure 3.13: 3D model of the PCB as implemented in HFSS.

Finally, the complete system was modeled by mounting the eWLB package onto the PCB structure - with the solder balls between. The solder balls were designed based on microscope measurements of their size. This setup enabled full-wave electromagnetic simulation of the antenna and interconnects in a realistic environment, including interfaces between the Vivaldi antenna, eWLB package, and PCB. Figure 3.14 shows the integrated model. In Figure 3.15, a transparent model is presented to show the vias.

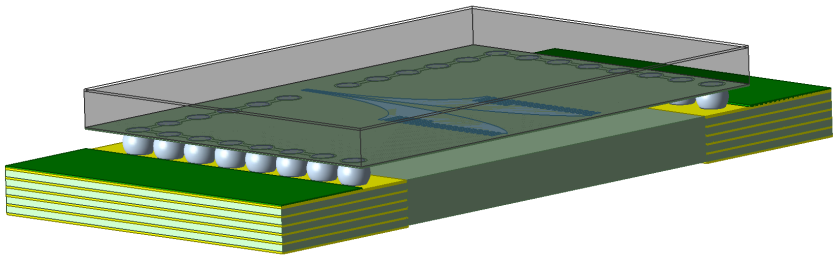

Figure 3.14: Integrated simulation model of the eWLB package mounted onto the PCB.

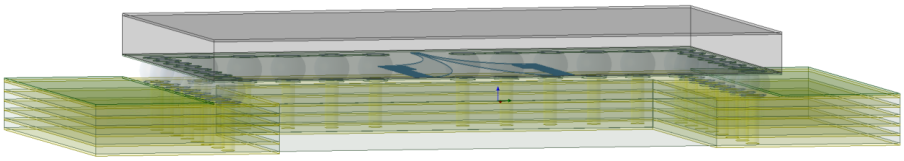

Figure 3.15: Transparent simulation model of the eWLB package mounted onto the PCB.

3.4 eWLB on PCB simulations

The Vivaldi antenna is excited by a terminal lumped port in between the two conductors to mimic a differential excitation and launching a quasi-TEM mode that propgates along the tapered slotline. The near-field Poynting field radiated from the integrated antenna is plotted in Figure 3.16, demonstrating the direction of the radiated power.

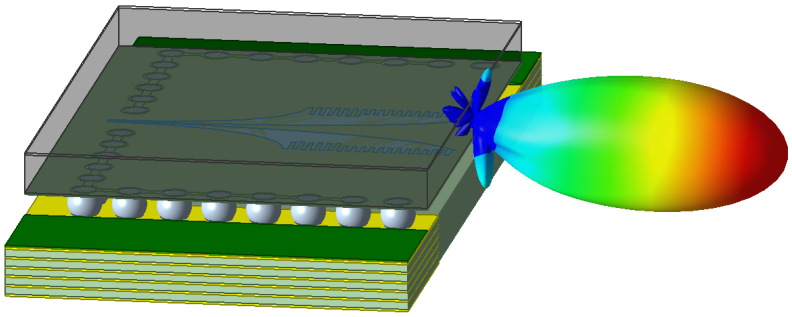

Figure 3.16: Near-field Poynting field radiated from the eWLB on PCB at 140 GHz.

The radiation pattern of the integrated antenna is plotted in Figure 3.17. A maximum gain in the E-plane of 9.4 dB is obtained, and the main direction of radiation is $\theta = 94.5°$, defined from the plane of the antenna.

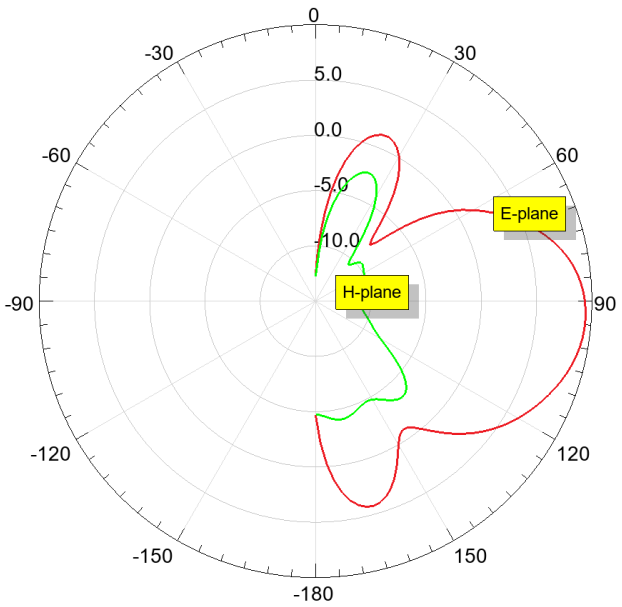

Figure 3.17: Radiation pattern of the integrated antenna at 140 GHz.

The electric field magnitude at the cross-section in front of the eWLB package, is plotted in Figure 3.18. The circle of which the field is plotted has the same size as the PMF to demonstrate how the field that would excite the PMF looks.

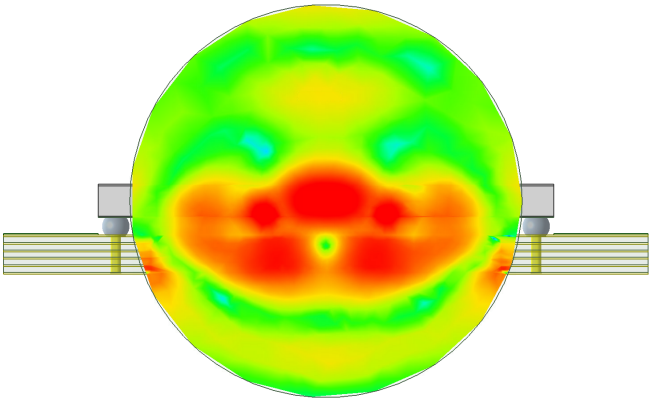

Figure 3.18: Cross-sectional electric field magnitude in front of the eWLB package at 140 GHz.

This field pattern does not match the field distribution of the propagating mode in the PMF, which contributes to the poor coupling observed.

3.5 Coupling simulations

To evaluate the coupling between the in-package Vivaldi antenna and the PMF, the full model was extended to include the PMF placed directly in front of the antenna aperture. The PMF was positioned along the endfire direction of the antenna, aligned for optimal excitation of the PMF. The coupling model includes all relevant structures, such as the eWLB package, PCB, and PMF, enabling simulation of energy transfer from the antenna into the PMF.
Figure 3.19 shows the simulation model used to analyze the coupling between the antenna and the PMF in a back-to-back configuration. This setup allows for accurate excitation of the PMF, and is used to analyze coupling losses and field patterns.

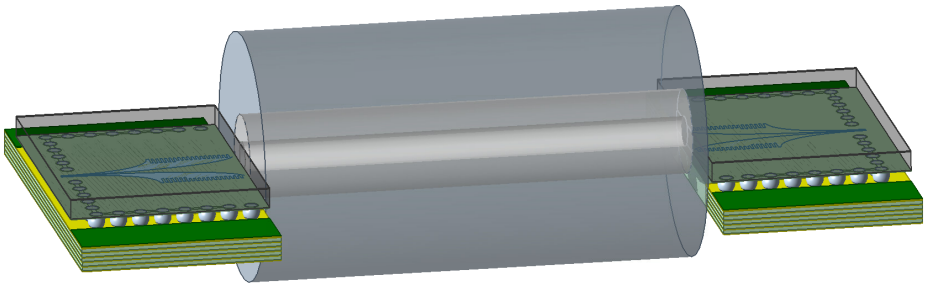

Figure 3.19: Back-to-back simulation setup showing two Vivaldi antenna structures with PMF between them.

A cross-section of the electric field magnitude at the center of the structure, showing how the electric field magnitude is propagating through the structure, is plotted in Figure 3.20. From this Figure, it is also clear that energy is leaking both upwards

through the eWLB, and downwards through the cavity on the PCB in undesired directions. It is also seen that the power is not well confined within the core of the PMF, which is not optimal.

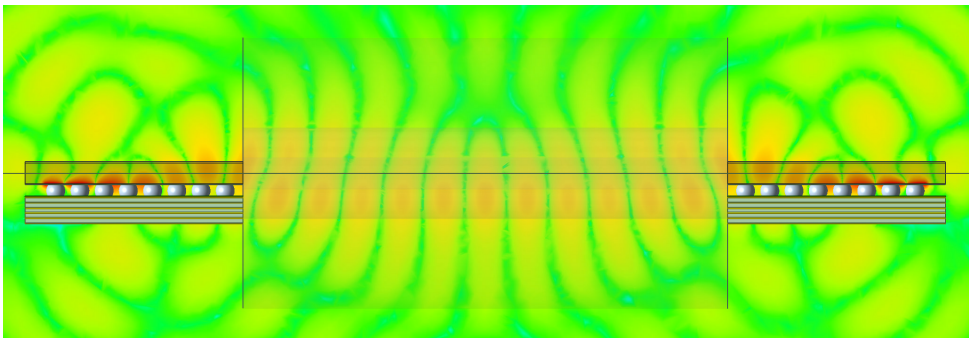

Figure 3.20: Cross-sectional electric field magnitude at the center of the back-to-back setup at 140 GHz.

Both the reflection coefficient (S_{11}) and the transmission coefficient (S_{21}) of the back-to-back simulation without the coupler are shown in Figure 3.21(a). S_{21} includes two transition losses and 10 mm of PMF loss, and the ports are defined as terminal lumped ports at the entrance of each antenna. By de-embedding the loss of a 10 mm long PMF—using the simulated S_{21} of the PMF itself—and dividing by two, the loss of a single transition can be extracted. The resulting coupling loss per transition is presented in Figure 3.21(b).

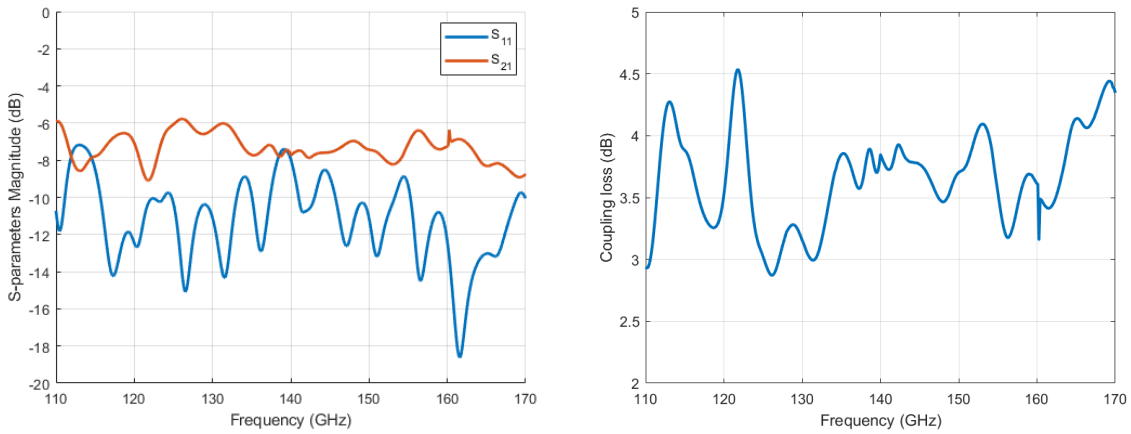

(a) S-parameters of the back-to-back simulation without coupler.

(b) Extracted coupling loss of a single transition without coupler.

Figure 3.21: Performance of the transition without coupler: (a) S-parameters of the back-to-back simulation and (b) corresponding single-transition coupling loss.

3.6 Alignment sensitivity simulations

To evaluate the robustness of the coupling structure to mechanical misalignment, a sensitivity analysis was performed for both lateral, vertical, and longitudinal displacement of the PMF relative to the eWLB package. Figure 3.22(a) shows the effect of lateral misalignment, where the PMF is shifted laterally across the aperture. Figure 3.22(b) illustrates the impact of vertical displacement, where the PMF is being shifted up and down. Figure 3.23 shows the effect of the PMF being shifted in the longitudinal dimension, leaving an air-gap in between the eWLB package and the PMF. For all cases, 0 mm means perfect alignment.

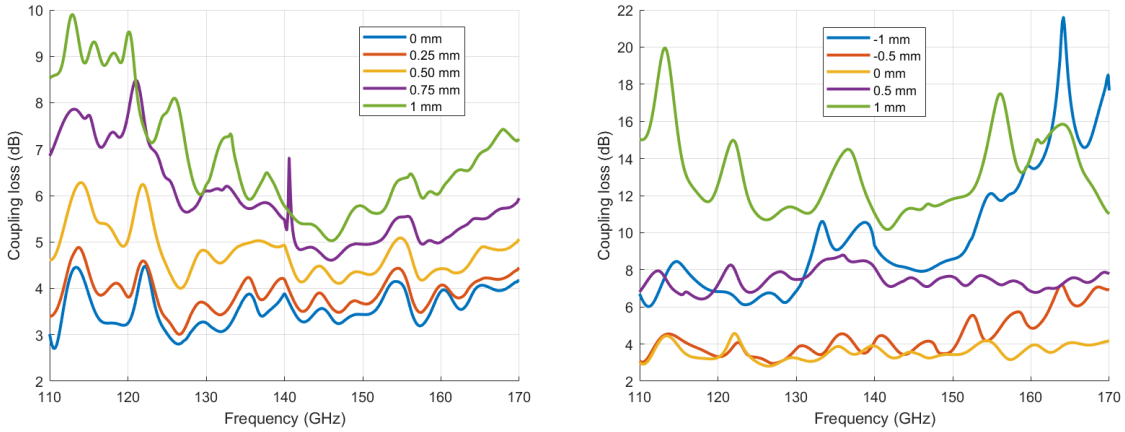

(a) Coupling loss as a function of lateral displacement of the PMF.

(b) Coupling loss as a function of vertical displacement of the PMF.

Figure 3.22: Sensitivity analysis of the coupler: (a) Lateral misalignment and (b) Vertical displacement between the PMF and the eWLB package.

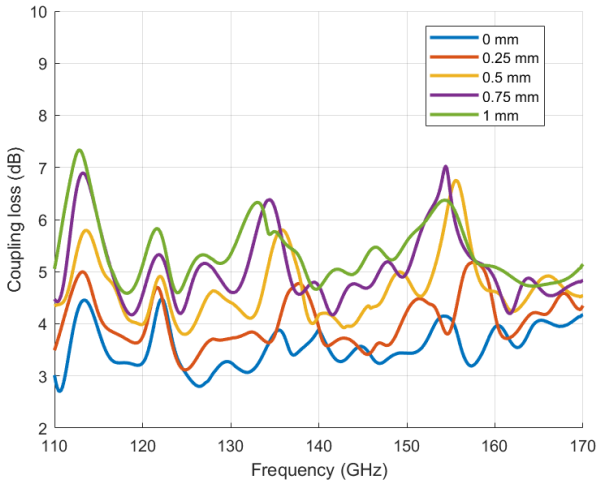

Figure 3.23: Coupling loss for longitudinal misalignment of the PMF.

4

Coupler design and optimization

This chapter introduces the design and simulation of a dielectric coupling structure intended to improve the transition between the embedded Vivaldi antenna in the eWLB package and the PMF. The proposed structure is designed to better confine the electromagnetic field and improve alignment with the modal profile of the PMF, aiming to reduce transition losses. The chapter includes the design and modeling approach using full-wave electromagnetic simulations, and the evaluation of field distributions and coupling efficiency. A back-to-back simulation setup is used to analyze the overall coupling performance.

4.1 Coupler design

The previous chapter shows that a significant portion of the power is radiated in unintended directions, and that the cross-sectional electric field magnitude does not match the field distribution of the PMF's fundamental mode. This means that a lot of the power that is radiated towards the PMF, will not excite it, and will instead lead to reflections.
By working with the simplest design possible, adding a structure on top of the eWLB package, to confine the leaking field within that structure, as well as having a structure between the eWLB package and the PMF, to help shaping the wavefront to match the propagating in the PMF, an increase in coupling is expected. The first prototype of this coupler is presented in Figure 4.1, and Figure 4.2 shows how the coupler is placed on the eWLB package.

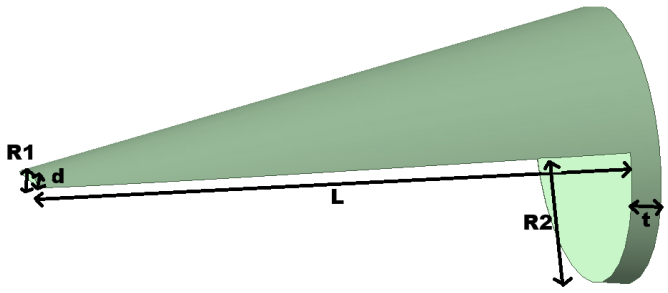

Figure 4.1: The coupler prototype with dimensions.

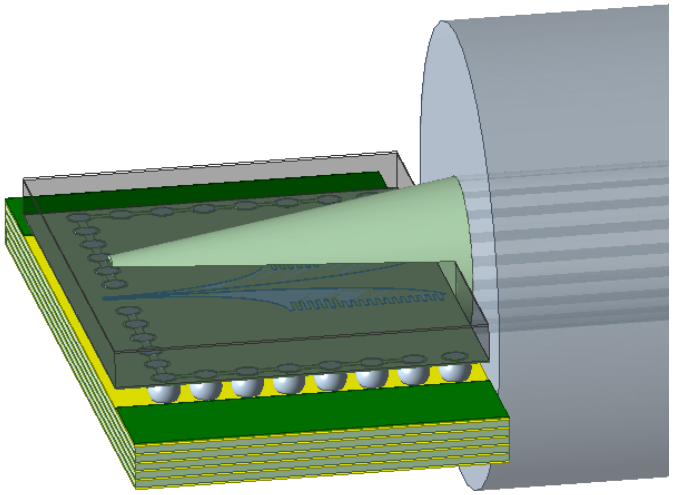

Figure 4.2: Prototype of the coupler mounted on the eWLB package.

The idea with this conical structure is to match the radius of the part of the coupler closest to the PMF, with the radius of the core of the PMF, since that is where the field should propagate. This large circle in front of the eWLB package will shape the field into a circular pattern - matching the PMF core. The tapered part above the eWLB package is both used to minimize the leakage of field through the package, as well as guiding it towards the PMF. By having this structure mounted, the leakage through the PCB cavity is also reduced due to more energy is confined within the upper part of the structure. The 4 mm long coupler is motivated by the length of the Vivaldi antenna - which is close to 4 mm. The small value of R_1 is chosen to minimize dielectric losses and the value of the thickness of the edge, d, is a consequence of the placement of R_1, and that the conical structure is cut to be placed on the eWLB package and PCB. The thickness of the section in front of the eWLB package, t, is chosen to be very thin, to minimize dielectric losses. The initial design parameters of the coupler are chosen as in Table 4.1.

Table 4.1: Initial design parameters of the coupler.

R_1 **[mm]**	R_2 **[mm]**	**L [mm]**	**d [mm]**	**t [mm]**
0.3	0.95	4	0.06	0.1

Depending on what material is chosen for the coupler, the field will be shaped differently. Having a dielectric with a higher dielectric constant will make the field stronger within the coupler, and by that, making it weaker in other parts of the eWLB package and the PCB. The cross-sectional electric field magnitude is plotted at the entrance of the PMF in Figure 4.3 for different dielectric constants of the coupler. The dielectric constant in the range 2-4 is chosen since that is a common range for standard 3D-printable dielectrics, which is planed to be used for this work.

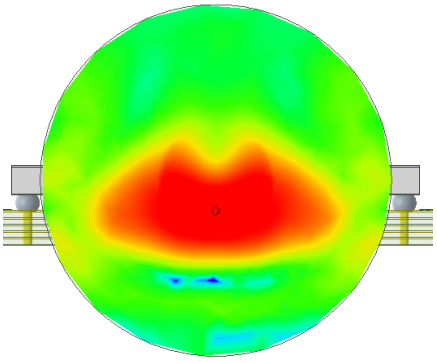

(a) Dk = 2.

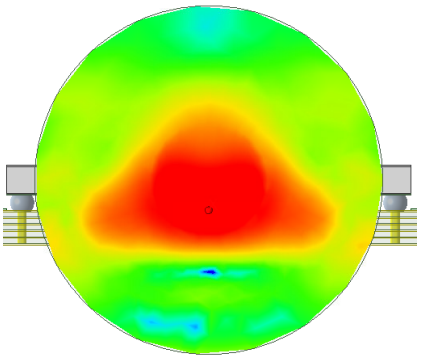

(b) Dk = 2.5.

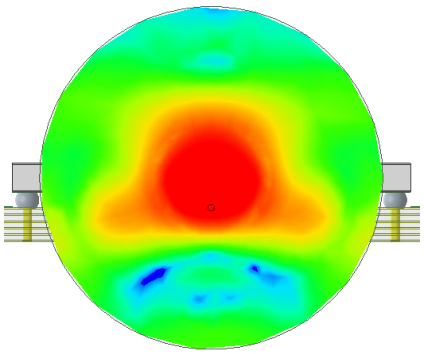

(c) Dk = 3.

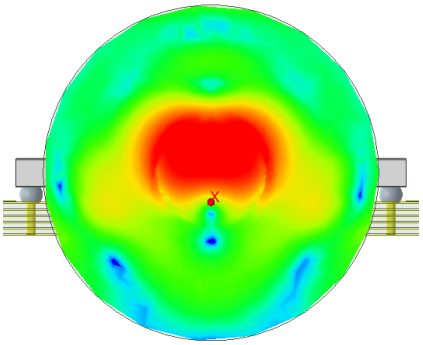

(d) Dk = 4.

Figure 4.3: Cross-sectional electric field magnitude in the plane of the PMF entrance for different dielectric constants of the coupler at 140 GHz.

A higher dielectric constant in the coupler results in a stronger electric field within the structure, thereby confining more of the field to the upper part of the coupler.

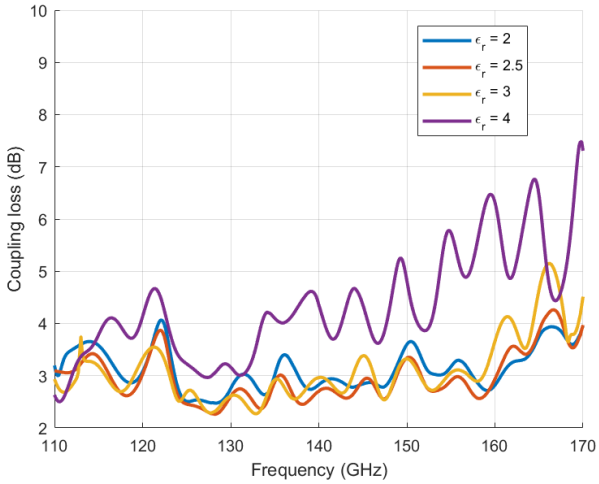

Figure 4.4: Coupling loss for varying dieletric constant of the coupler.

For this specific design of the coupler, having a higher dielectric constant of 4, is not effective, since it suffers from both larger loss and greater frequency dependence. Choosing a dielectric constant between 2-3 is better, where the lower dielectric constant, the less frequency dependence. One of the standard 3D-printing materials, Acrylonitrile Butadiene Styrene (ABS), has an approximate dielectric constant of 2.35 and a dielectric loss tangent of 0.005 at D-band frequencies [19]. Since ABS has great electromagnetic performance at D-band frequencies, and the possibility to print with an advanced printer in ABS at Ericsson, motivates the use of ABS for this work. In Figure 4.5, the electric field magnitude is plotted at the cross-section of the entrance to the PMF, when ABS is used.

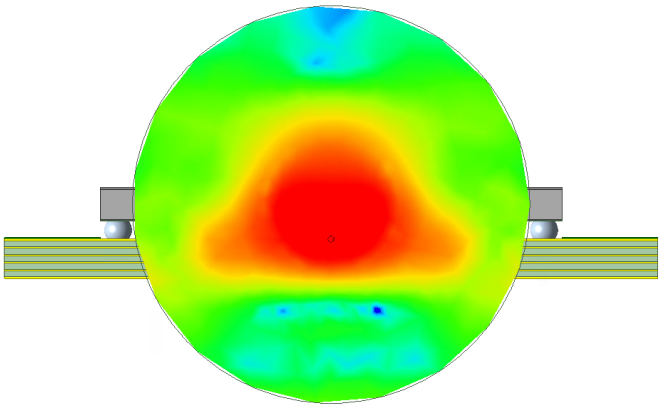

Figure 4.5: Cross-sectional electric field magnitude for the coupler in ABS at 140 GHz.

A cross-section of the electric field magnitude at the center of the structure, showing how the electric field magnitude is propagating through the structure, is plotted in Figure 4.6. The plot shows that there is reduced field leakage through the eWLB package and the PCB, along with fewer reflections at the PMF interface. It also demonstrates that the PMF is excited without any angular offset, which minimizes propagation in the cladding and results in greater energy confinement within the core.

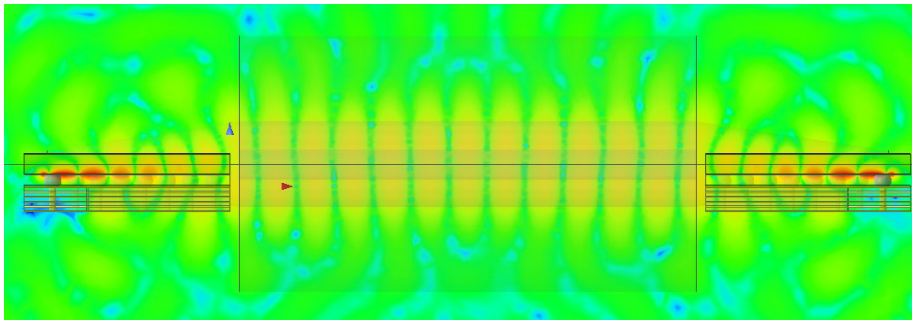

Figure 4.6: Cross-sectional electric field magnitude at the center of the back-to-back setup with the coupler at 140 GHz.

S_{11} and S_{21} of the back-to-back simulation setup are presented in Figure 4.7. An improvement in S_{21} is observed, indicating enhanced coupling efficiency, while a slight degradation in S_{11} is noticeable - compared with the without coupler case. The degradation in S_{11} is likely caused by the added dielectric structure, which introduces dielectric loading to the antenna, which affects the impedance matching. The resulting coupling loss of a single transition is shown in Figure 4.7(b).

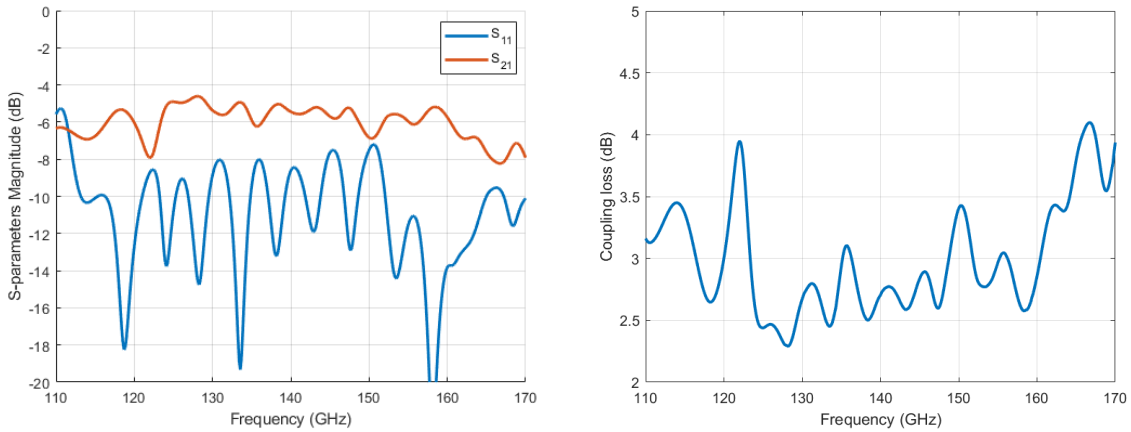

(a) S-parameters of the back-to-back coupler simulation.

(b) Coupling loss of a single transition with the coupler.

Figure 4.7: Performance of the dielectric coupling structure: (a) S-parameters and (b) Extracted single-transition coupling loss.

4.2 Coupler optimization

The different parameters of the coupler are investigated in order to find the optimal design for the lowest coupling loss. A coupler of the type presented in Section 4.1 is now investigated, where ABS is used as the material. In Figure 4.8, the radius of the section that is closest to the PMF is varied - to find the most promising value of the radius. Choosing a radius close to or slightly larger than that of the PMF core appears to be an effective design choice. Hence, choose a value of $RAD_2 = 1.15$ mm.

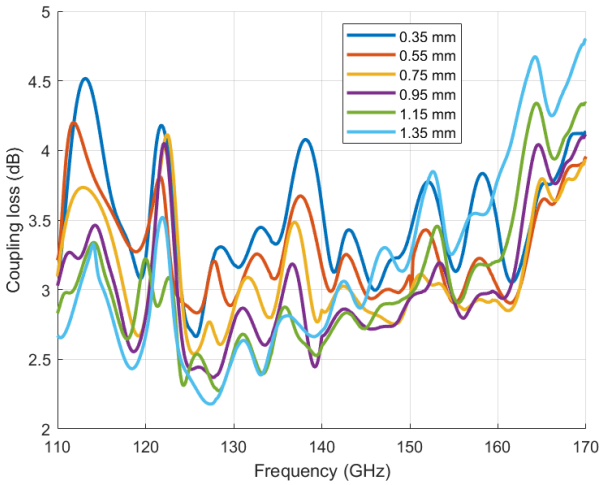

Figure 4.8: Coupling loss for radius sweep of the part of the coupler closest to the PMF.

With RAD_2 set to 1.15 mm, the influence of the radius of the smaller circle at the other end of the coupler is swept. It is clear from Figure 4.9 that the smaller the value of RAD_2, the better. For the printer used in this work, one single layer is 0.127 mm thick, which means that d = 0.127 mm is the thinnest we can fabricate. By choosing d = 0.127 mm, the corresponding RAD_2 is then 0.367 mm.

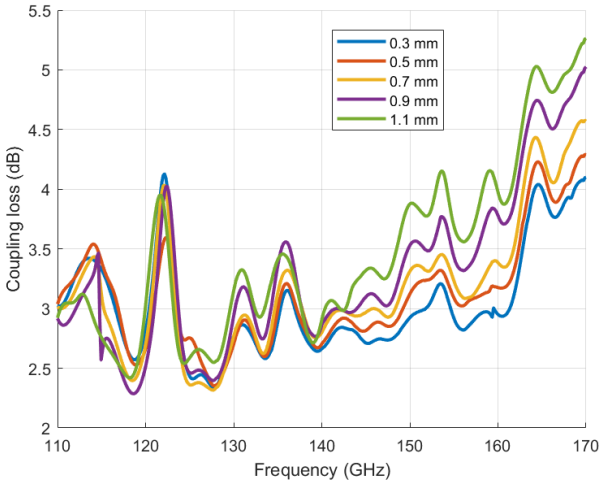

Figure 4.9: Coupling loss for radius sweep of the part of the coupler furthest away from the PMF.

For $RAD_1 = 0.367$ mm and $RAD_2 = 1.15$ mm, the length of the coupler is swept in Figure 4.10. The most promising length of the coupler is 2.5 mm for a broadband and low coupling loss.

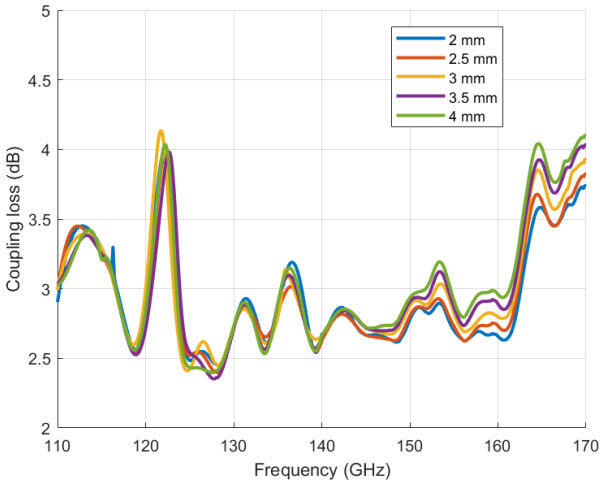

Figure 4.10: Coupling loss for coupler length sweep.

For all the above parameter sweeps, the coupler thickness towards the PMF, t, was kept constant at 0.1 mm. However, to ensure compatibility with the mechanical fixture holding the coupler in place, the thickness had to be increased. A final thickness of 0.5 mm was selected to provide sufficient mechanical stability. The coupler dimensions after parametric sweeps and thickness adjustment are shown in Table 4.2. The updated S-parameters and corresponding coupling loss are presented in Figure 4.11.

Table 4.2: Design parameters of the coupler after parametric sweeps.

R_1 [mm]	R_2 [mm]	L [mm]	d [mm]	t [mm]
0.367	1.15	2.5	0.127	0.5

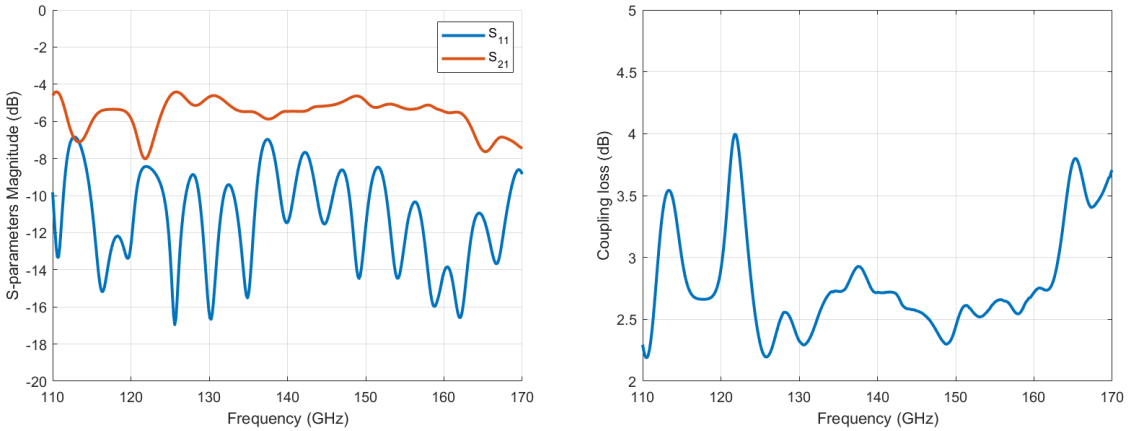

(a) S-parameter magnitude of the new coupler.

(b) Coupling loss of the new coupler.

Figure 4.11: Performance of the coupler after parametric sweeps: (a) S-parameters and (b) Coupling loss.

To further enhance the coupling and minimize coupling loss in the 130–150 GHz frequency range, all coupler parameters were optimized using HFSS. Small adjustments in all parameters are made to find the lowest coupling loss in the frequency range of interest. The S-parameters and corresponding coupling loss are presented in Figure 4.12 for the optimized coupler. The design parameters of the coupler after optimization are presented in Table 4.3.

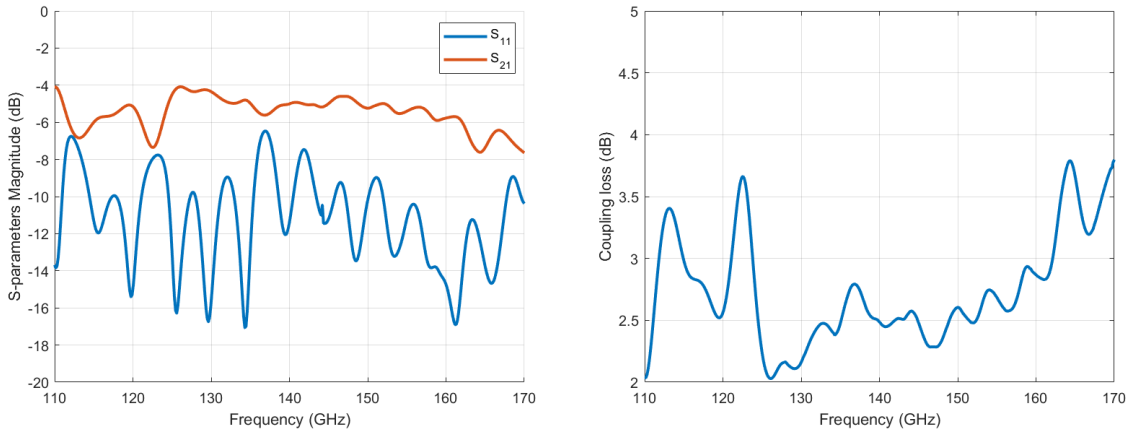

(a) S-parameter magnitude of the optimized coupler.

(b) Coupling loss of the optimized coupler.

Figure 4.12: Performance of the optimized coupler design (a) S-parameters and (b) Coupling loss.

Table 4.3: Design parameters of the coupler after optimization.

R_1 **[mm]**	R_2 **[mm]**	**L [mm]**	**d [mm]**	**t [mm]**
0.367	1.2	2.4	0.127	0.5

4.3 Coupler as a connector

There are pre-defined holes in the PCB, as can be seen in Figure 4.13 of the PCB layout. These holes can be used to mount a fixture for the PMF onto the PCB. This type of fixture helps hold the PMF in place, which would solve the problem with misalignment. The model of the proposed fixture is presented in Figure 4.14.

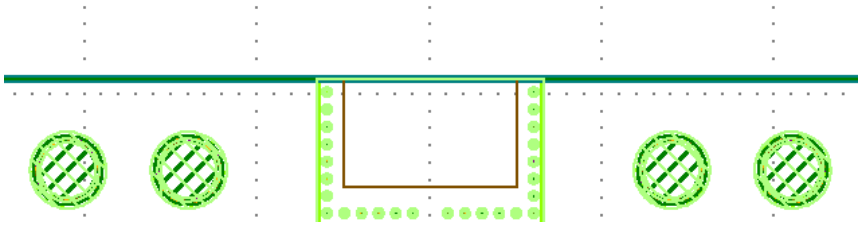

Figure 4.13: PCB layout showing the holes used for mounting the fixture.

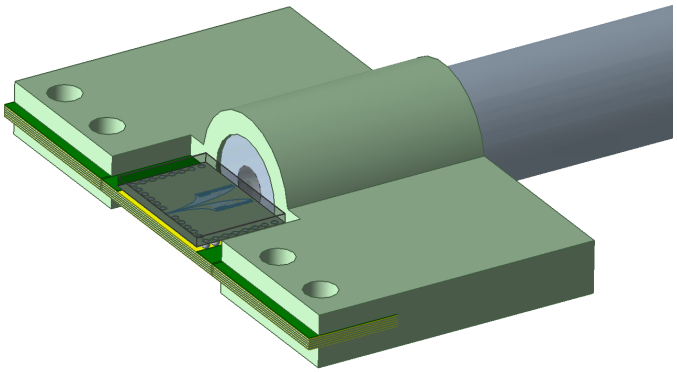

Figure 4.14: Fixture model on PCB holding the PMF.

The purpose of the fixture is not only to hold the PMF in place, but also to integrate it together with the coupler, so that also the coupler will be kept in place. Figure 4.15 shows how this can be done. This structure has easy integration with both the PMF and PCB, as well as improving the coupling between the eWLB package and the PMF by integrating the coupler into it. A ring that stops the PMF from going through the fixture and pins for holding the coupler in place is added to the fixture. For this, both mechanical and electromagnetic design had to be taken into account, in order to fabricate o robust coupler with great performance.

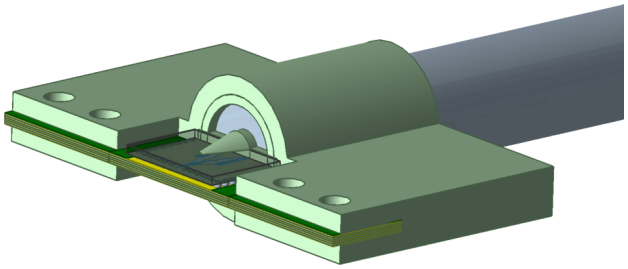

Figure 4.15: Fixture model with integrated coupler.

The S-parameters of the fixture with the integrated coupler are shown in Figure 4.16(a), and the resulting coupling loss is presented in Figure 4.16(b). These figures show the simulation results of the coupler that is fabricated.

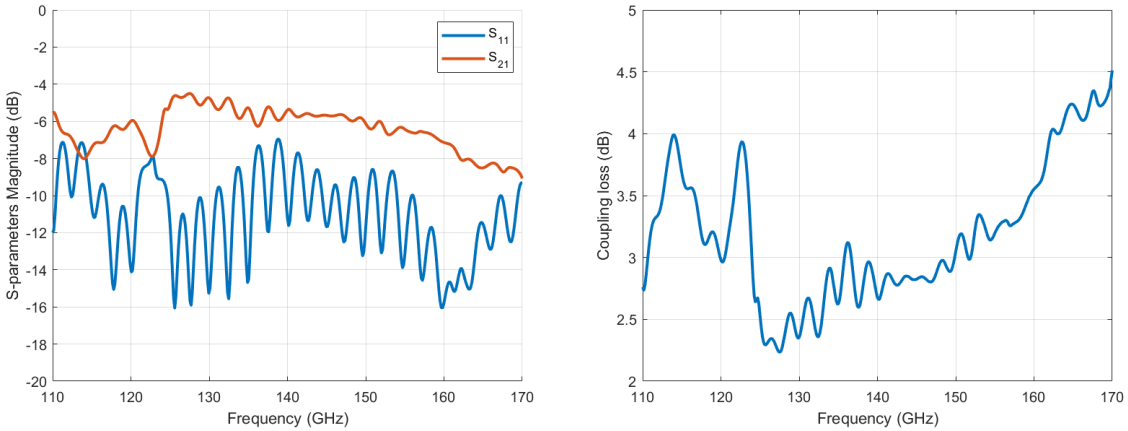

(a) S-parameters of the coupler integrated in the fixture.

(b) Coupling loss with the coupler integrated in the fixture.

Figure 4.16: Simulated performance of the coupler integrated into the full fixture: (a) S-parameters and (b) Coupling loss.

Figure 4.17(a) shows a comparison of the simulated coupling loss for the with- and without coupler case, and Figure 4.17(b) shows the improvement in the simulated coupling with the coupler. The simulated coupling improvement in the 130-150 GHz frequency range is between 0.35-1.25 dB.

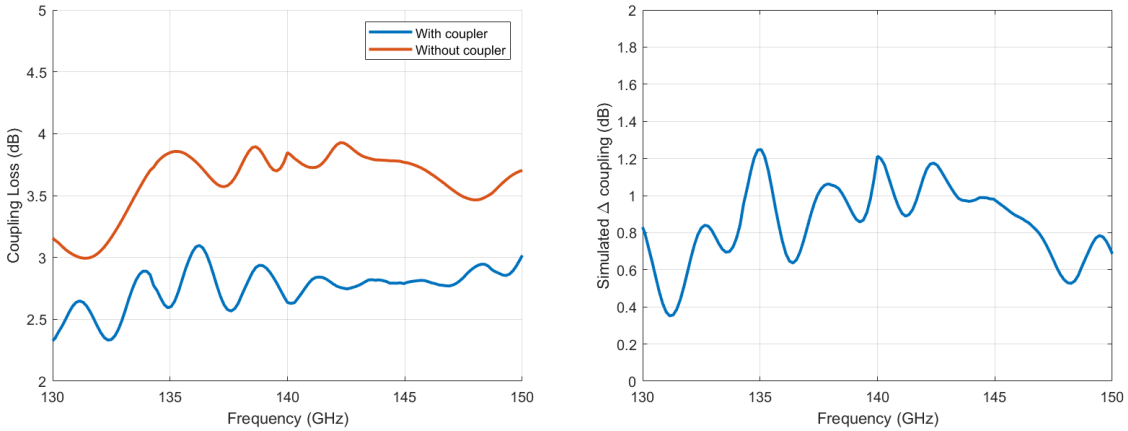

(a) Simulated coupling loss with- and without the coupler.

(b) Simulated coupling improvement with the coupler.

Figure 4.17: Simulated performance of the coupler integrated into the full fixture: (a) S-parameters and (b) Coupling loss.

Due to imperfect fabrication, a perfect contact between the eWLB package and the coupler is not expected, which motivates the simulations of an air gap between the coupler and the eWLB package. Figure 4.18 shows the gap investigated. In the simulations it means that the coupler is being shifted upwards.

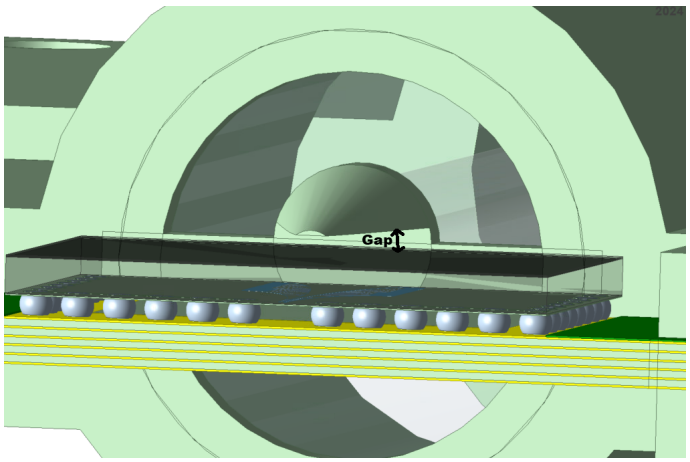

Figure 4.18: Air gap between the coupler and the eWLB package.

Figure 4.19 shows how the air gap affects the simulated coupling loss. It shows that having no air gap performs worse than having air gaps in the range 50-200 μm. The best performance is obtained when there is 100 μm air gap in between the coupler and the eWLB package. The simulated coupling improvement in the 130-150 GHz frequency range is between 0.4-1.4 dB with the air gap being 100 μm.

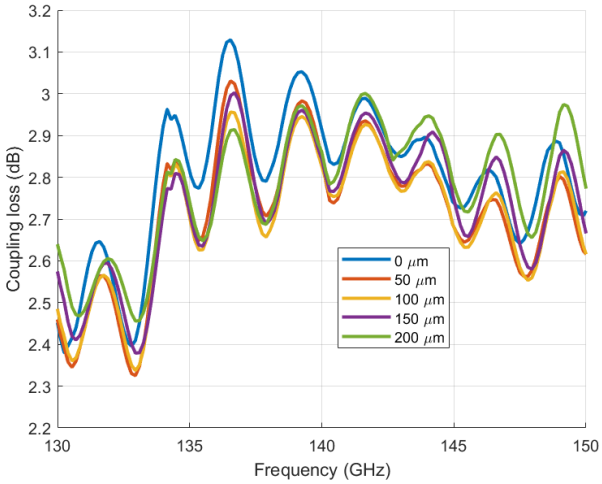

Figure 4.19: Coupling loss for varying air gap.

5
Fabrication and measurements

This chapter presents the process of fabricating and experimentally validating the 3D-printed coupler developed to improve electromagnetic coupling between the eWLB package and the PMF. The first part describes the fabrication, which was carried out using high-resolution 3D printing. To ensure that the printed part matched the original design, it was examined under a microscope. The second part focuses on the measurements performed to evaluate the coupler's performance. Measurements of the transmission coefficient were carried out with and without the coupler in place, allowing to extract the difference in coupling, with and without the coupler.

5.1 Fabrication process

The structure was fabricated using a Stratasys F370 3D-printer with ABS as the printing material. The layering thickness of the 3D-printer is 0.127 mm, which was considered in the design process to preserve the coupler geometry. Once printing was complete, the part was submerged in an ORYX SCA3600 with chemical bath to dissolve the support material used by the printer.
After fabrication, inspection was carried out under a digital microscope after the coupler was mounted on the PCB with the eWLB package mounted. Figure 5.1 shows the difference in distance between different surfaces from a top view. From this figure, the width of the coupler could easily by extracted at the two different cuts along the width of the coupler. By taking the difference in position along the width between the sharp edges, corresponding to the coupler's edge, the width at that certain cut was obtained.

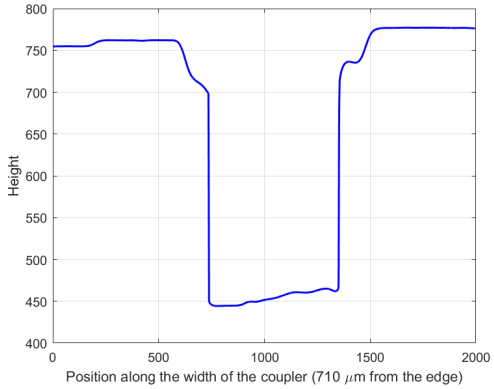

(a) Thickness profile of the coupler in the width direction (710 μm from the edge).

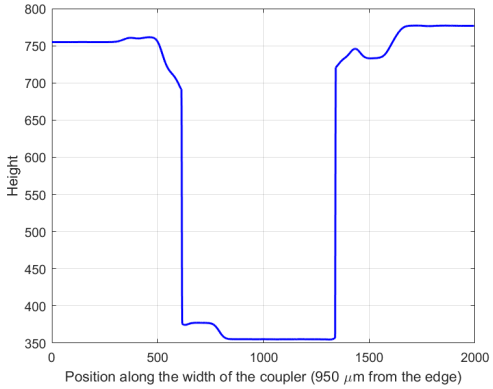

(b) Thickness profile of the coupler in the width direction (950 μm from the edge).

Figure 5.1: Thickness profile of the coupler in the width direction: (a) 710 μm from the edge and (b) 950 μm from the edge.

By comparing the height difference in Figure 5.1 between the eWLB surface (corresponding to the maximum value), and the heighest point on the coupler (corresponding to the mimimum value), and subtracting the thickness value from the model of the coupler at that position, the air gap is obtained. Since there are two different cuts, this process was done for both cuts. In the Table 5.1 the height difference, the coupler thickness, and the resulting air gap are presented for the two cuts. An average air gap of 98 μm is observed. From previous simulations, we know that a small air gap between this coupler and the eWLB package results in better coupling.

Table 5.1: Measured and modeled coupler thickness at two cross-sections, and resulting air gap.

Cut [μm]	**Height difference [μm]**	**Coupler thickness [μm]**	**Air Gap [μm]**
710	327	245	82
950	422	307	115

Figure 5.2 shows an image of the tip of the coupler made by the microscope, which shows the defects coming from the printer. The thickness does not increase smoothly along the length; instead, discrete height steps are observed, corresponding to the thickness of each layer deposited by the printer.

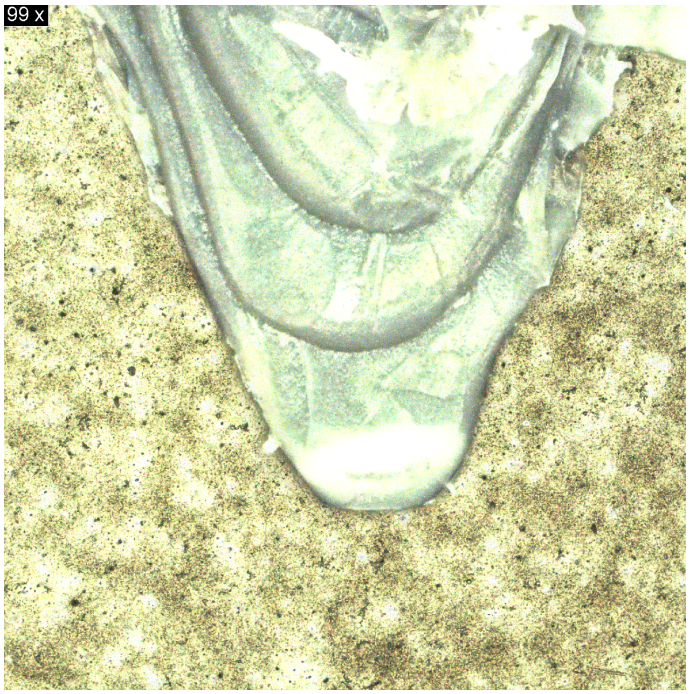

Figure 5.2: Microscope image of the tip of the coupler.

5.2 Coupling measurements

The measuring setup presented in Figure 5.3 is used for the following measurements. The measurements are done to investigate how much better the coupling is with the coupler compared to without it. S_{21} measurements were first performed without the coupler being mounted. Later, the coupler was mounted and the S_{21} was measured again.

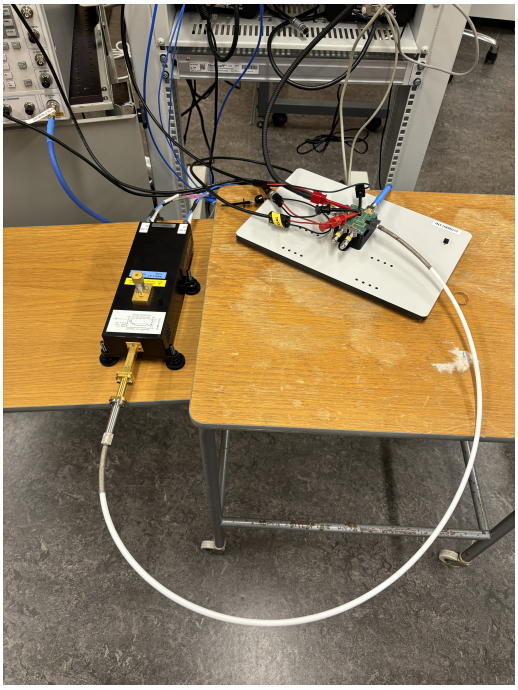

Figure 5.3: Measurement setup for measuring the S_{21} with- and without the coupler.

The S_{21} measurements for the with- and without-coupler cases are plotted in Figure 5.4 in the 130-150 GHz range, which is of most interest. With this specific PCB and eWLB package, it is not possible to directly probe the antenna and measure the absolute coupling value. Instead, the S_{21} measurement represents the full transmission channel, including waveguide-to-PMF losses, PCB and eWLB losses, and on-chip amplifier gains. However, the only difference between the two measurements is the presence of the coupler in one of them. This makes it possible to extract the improvement in coupling when using the coupler, rather than determining the absolute coupling value. The measurements suffer from large ripples, which makes it difficult to obtain exact coupling improvement values. The measured coupling improvement in the frequency range 130-140 GHz is between 0.5-2.2 dB.

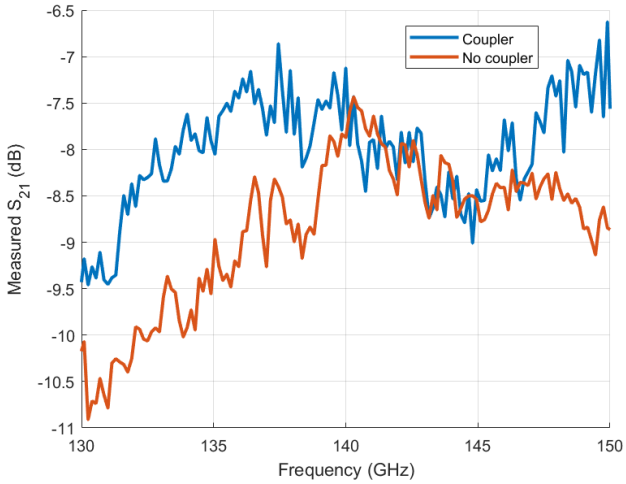

Figure 5.4: Measured S_{21} with- and without the coupler.

6
Conclusion and future outlook

6.1 Conclusion

The measured coupling improvement across the frequency range 130-140 GHz when mounting the coupler on the eWLB package is between 0.5-2.2 dB. The designed coupler not only gives an improvement in coupling, but also offers a compact solution to hold the PMF in front of the eWLB package. Simulations of the same coupler show a coupling improvement across the frequency range 130-150 GHz between 0.4-1.4 dB. This indicates that the simulated coupler is more broadband but provides less coupling improvement compared to the measured coupler. This is likely due to fabrication issues of the coupler, such as discrete thickness increase due to layering in 3D printing, rough surfaces and imperfect contact between the coupler and the PMF.

6.2 Future outlook

A potential area for future improvement is the joint optimization of the coupler and the fixture, possibly including a complete redesign of the integration concept. The use of a Graded-Index (GRIN) lens integrated above the eWLB package could be explored in more detail since it has great potential of shaping the field. Having a coupler both above the eWLB package as in this work, and below the PCB cavity could be explored, even though more fabrication would be more difficult. Additionally, other types of dielectric lens structures placed in front of the eWLB package could be investigated to increase the directivity and gain of the integrated antenna. This could help concentrate more power into the desired propagation direction and thereby improve the overall coupling performance to the PMF.

Bibliography

[1] 6GTandem, “About 6GTandem,” Horizon 6GTandem, 2024. [Online]. Available: https://horizon-6gtandem.eu/about/. [Accessed: Jan. 31, 2025].

[2] Y. Cao, M. Wojnowski, and B. K. Lau, “Circularly polarized sub-THz antenna design for distributed deployment,” in *Proc. IEEE*, 2024. [Online]. Available: https://ieeexplore.ieee.org/document/xxxxx

[3] P. Reynaert *et al.*, "Polymer Microwave Fiber: A New Communication Concept That Blends Wireless, Wireline and Optical Communication," in *Proc. IEEE ICECS*, Nov. 2019.

[4] M. Wojnowski *et al.*, “Embedded Wafer Level Ball Grid Array (eWLB) Technology for Millimeter-Wave Applications,” in *Proc. 13th Electronics Packaging Technology Conference (EPTC)*, 2011.

[5] I. Ocket, M. Cauwe, and B. Nauwelaers, "Millimeter Wave Planar Transition from Plastic Rectangular Waveguide to 1 mm Coax," *Proc. 46th European Microwave Conference (EuMC)*, London, UK, Oct. 2016.

[6] A. Meyer, S. Karau, and M. Schneider, "Broadband Stacked-Patch Transition from Microstrip Line to Circular Dielectric Waveguide for Dual-Polarized Applications at W-Band Frequencies," *Proc. 49th European Microwave Conference (EuMC)*, Paris, France, Oct. 2019.

[7] A. Hassona, V. Vassilev, Z. S. He, A. Zaman, C. Mariotti, F. Dielacher, and H. Zirath, “D-band waveguide-to-microstrip transition implemented in eWLB packaging technology,” *Electronics Letters*, vol. 56, no. 4, pp. 187–189, Feb. 2020.

[8] H. Chang, V. Torres, S. An, F. Strömbeck, Y. Yan, H. Zirath, I. Papananos, J. Hansryd, and Y. Li, "D-band Data Interconnect Based on Polymer Microwave Fiber in SiGe HBT Technology," *Proc. 54th European Microwave Conference (EuMC)*, Paris, France, Sep. 2024.

[9] V. Liakonis, Y. Papananos, M. Wojnowski, and W. Hartner, "High-Performance Polymer Microwave Fiber Coupler in eWLB Package for Sub-THz Communication," in *Proc. 74th Electronic Components and Technology Conference (ECTC)*, IEEE, 2024.

[10] D. M. Pozar, *Microwave Engineering*, 4th ed. Hoboken, NJ: Wiley, 2012.

[11] B. E. A. Saleh and M. C. Teich, *Fundamentals of Photonics*, 3rd ed. Hoboken, NJ, USA: John Wiley Sons, 2019.

[12] M. Schneider and A. Meyer, “Normalized design charts for low-loss and dispersion-minimized circular dielectric waveguides for millimeter waves,” in *Proc. German Microwave Conference (GeMiC)*, Duisburg, Germany, Mar. 2024.

[13] P.-S. Kildal, *Foundations of Antenna Engineering*, Hoboken, NJ: Wiley, 2014.

[14] M. M. Rana, R. Khanom, and M. M. Rahman, “Design and Analysis of Vivaldi Antennas,” Dept. of Electronics and Communication Engineering, Khulna Univ. of Engineering Technology, Bangladesh, 2024.

[15] R. C. Johnson, “Slot Antennas,” in *Antenna Engineering Handbook*, 3rd ed. New York, NY: McGraw-Hill, 1993.

[16] P. J. Gibson, “The Vivaldi aerial,” in *Proc. 9th European Microwave Conference*, Brighton, UK, 1979, pp. 101–105.

[17] A. S. Dixit and S. Kumar, “A Survey of Performance Enhancement Techniques of Antipodal Vivaldi Antenna,” *IEEE Access*, vol. 8, pp. 45773–45794, 2020.

[18] R. Janaswamy and D. H. Schaubert, *Characteristic Impedance of a Wide Slot Line on Low Permittivity Substrates*, Univ. of Massachusetts, Amherst, 1985. [Unpublished].

[19] M. Funk *et al.*, “Ultra-Broadband Material Characterization in W- and D-Band Using a Free-Space Setup,” *2024 Int. Conf. on Electromagnetics in Advanced Applications (ICEAA)*, IEEE, 2024, pp. 288–290. doi:10.1109/ICEAA61917.2024.10701940.

DEPARTMENT OF SOME SUBJECT OR TECHNOLOGY
CHALMERS UNIVERSITY OF TECHNOLOGY
Gothenburg, Sweden
www.chalmers.se

CHALMERS
UNIVERSITY OF TECHNOLOGY